Geochemistry Geophysics Geosystems G3
AN ELECTRONIC JOURNAL OF THE EARTH SCIENCES
Published by AGU and the Geochemical Society

Article
Volume 10, Number 1
9 January 2009
Q01003, doi:10.1029/2008GC002143
ISSN: 1525-2027

Determination of the volcanostratigraphy of oceanic crust formed at superfast spreading ridge: Electrofacies analyses of ODP/IODP Hole 1256D

Masako Tominaga
Department of Oceanography, Texas A&M University, College Station, Texas 77843-3146, USA (masako@ocean.tamu.edu)

Damon A. H. Teagle
School of Ocean and Earth Science, National Oceanography Centre, University of Southampton, Southampton SO14 3ZH, UK

Jeffrey C. Alt
Department of Geosciences, University of Michigan, Ann Arbor, Michigan 48109, USA

Susumu Umino
Department of Earth Science, Kanazawa University, Kanazawa-Shi, Ishikawa 920-1192, Japan

[1] The objective of this study is to construct a representative volcanostratigraphy of Ocean Drilling Program Hole 1256D, the first complete penetration of intact upper oceanic crust formed at a superfast spreading rate. An accurate knowledge of the volcanostratigraphy is vital to understand processes of crustal construction and submarine magmatism and to estimate chemical exchange with seawater, but this is rarely achieved due to very low recovery rates in most basement holes. We used two approaches to determine the rock types that form the wall rocks in the basement sections of Hole 1256D: (1) user guided interpretations of electrofacies acquired by imaging tools combined with other wireline tools; and (2) the use of an artificial neutral network to objectively classify the responses of all available logging information. Great availability of formation microscanner (FMS) images provided superior coverage of the borehole wall compared to previous attempts at core-log integration. This has resulted in more confident and detailed lithologic classifications, such as with the distinction between pillows and different styles of breciation. Ten lithology types are suggested for a volcanostratigraphy model: massive flows, ponded lava, fractured massive flows, fragmented flows, thin flows or thick pillows, pillows, breccias, dikes in dike complex, isolated dikes, and gabbros. Three major lithology types in the extrusive section are massive flows (both massive and fragmented massive flow, 22%), fragmented flows (32%), and breccias (19%). Pillow lavas make up only 1.9% of the volcanic section and are confined to a 100 m interval. Below the extrusive section, subvertical contacts interpreted to be dike margins are typically observed every 1 to 2 m with brecciated zones along the contacts. The dikes dip steeply to the northeast indicating slight rotation away from the ridge axis. We used an artificial neural network (ANN) approach to determine a quantitative lithostratigraphy. The ANN is most strongly influenced by porosity and alteration degrees and the resulting stratigraphy most closely resembles the above classifications when clustered by FMS texture as opposed to lithologic interpretation. The ANN thus provides a porosity-based stratigraphy of the basement rather than the traditional lithology-based stratigraphy.

Components: 13,062 words, 12 figures, 4 tables.

Keywords: Integrated Ocean Drilling Program; Hole 1256D; electrofacies analyses; volcanostratigraphy; artificial neural network.

Index Terms: 3036 Marine Geology and Geophysics: Ocean drilling; 3035 Marine Geology and Geophysics: Midocean ridge processes; 3045 Marine Geology and Geophysics: Seafloor morphology, geology, and geophysics.

Received 30 June 2008; **Revised** 31 October 2008; **Accepted** 13 November 2008; **Published** 9 January 2009.

Tominaga, M., D. A. H. Teagle, J. C. Alt, and S. Umino (2009), Determination of the volcanostratigraphy of oceanic crust formed at superfast spreading ridge: Electrofacies analyses of ODP/IODP Hole 1256D, *Geochem. Geophys. Geosyst.*, *10*, Q01003, doi:10.1029/2008GC002143.

1. Introduction

[2] An accurate downhole lithostratigraphy provides the basic foundation for interpreting any section of drilled oceanic crust. However, reconstructing the distribution of rock types downhole remains one of the major challenges to hard rock ocean drilling. This is because core recovery rates in the upper oceanic crust are typically low (<30%) with few long continuous core pieces, and better-drilled rock types (i.e., less fractured rocks) are preferentially recovered. Volcanostratigraphy models derived solely from recovered cores thus only partially represent the basement and are generally strongly biased against more fragile rock types such as highly altered and fractured formations, breccias, and fracture fills. With such low recovery rates, there is significant uncertainty as to the original in situ location of the core pieces recovered, so the unrecovered rock formations must be interpolated from the recovered rock types. Consequently, core-based volcanostratigraphic models may lead to erroneous classifications of lithologic types, misinterpretations of crustal construction processes, and inaccurate estimates of seawater-basalt chemical exchange fluxes resulting from hydrothermal alteration [e.g., *Alt and Teagle*, 1999; *Teagle et al.*, 1998, 2003; *Fisher*, 2004; *Nielsen et al.*, 2006]. An alternative to the current approach of developing crustal stratigraphies solely from the recovered cores is essential.

[3] In this study, we present a qualitative electrofacies analysis of in situ wireline logs integrated with observations of the recovered cores to reconstruct an igneous stratigraphy model of the intact upper oceanic crust in Ocean Drilling Program/Integrated Ocean Drilling Program (ODP/IODP) Hole 1256D. We further investigated quantitative wireline log analysis through the use of unsupervised artificial neural network (ANN) methods to automatically and objectively construct a quantitative volcanic stratigraphy model. We compare the results of the ANN technique with our qualitative electrofacies analysis to investigate the characteristics of each approach and discuss how we can utilize these qualitative and quantitative analyses to improve the construction of a volcanostratigraphy model. Testing the quantitative approach is important to consider if semi-automated lithostratigraphy modeling immediately at the completion of logging operations onboard is possible and informative. Companion papers will discuss the geological implications of the basement volcanostratigraphy developed here with respect to the accretion of the upper crust at Site 1256, the implications for crustal magnetism, and hydrothermal chemical exchange.

2. Background

2.1. Geological Background

[4] ODP/IODP Hole 1256D (6°44.1 N, 91°56.1) is located in the Guatemala Basin on the eastern flank of the East Pacific Rise (EPR). Marine magnetic anomalies indicate that the crust was accreted ~15 Ma during an episode of superfast spreading (full > 220 mm/a, Figure 1) [*Wilson*, 1996]. The location of Hole 1256D was specifically sited to (1) drill the first continuous section of intact upper oceanic crust down to gabbros, (2) test the correlation between the increasing spreading rate and the decreasing depth to the axial low-velocity zones thought to be axial melt lenses and now preserved as gabbros [e.g., *Purdy et al.*, 1992], (3) determine the lithology and structure of the upper oceanic crust from a super-fast spreading rate end-member, (4) examine the seismic and magnetic structure of the upper oceanic crust, and (5) inves-

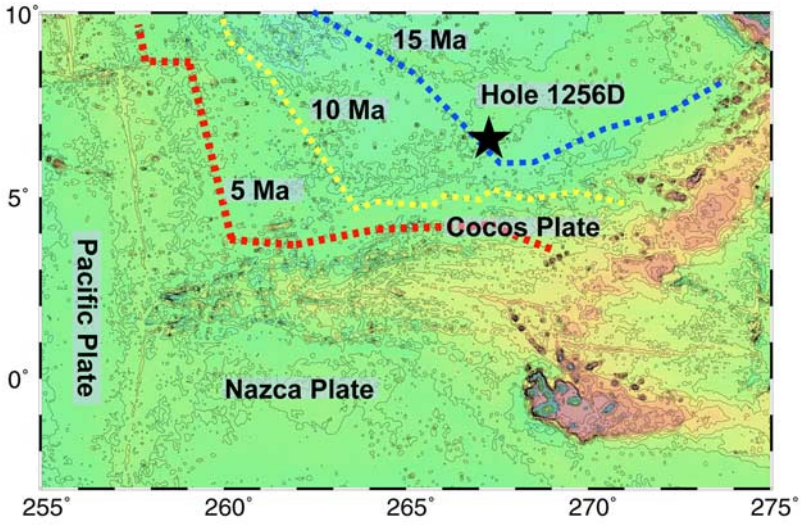

Figure 1. Predicted bathymetry map of the Cocos-Nazca-Pacific region and location of ODP/IODP Hole 1256D [*Smith and Sandwell*, 1997]. Red and blue dashed lines indicate 10 and 15 Ma isochrons, respectively.

tigate magmatic and alteration processes through intact upper oceanic crust. Drilling at Site 1256 was initiated on ODP Leg 206 [*Wilson et al.*, 2003] and continued on IODP Expeditions 309 and 312 [*Teagle et al.*, 2006]. Hole 1256D now penetrates 1507.1 m below seafloor (mbsf; 1257 m subbasement (msb)) with the first gabbroic rocks recovered at 1407 mbsf. The preliminary downhole stratigraphy established from shipboard core observations and wireline log interpretations onboard revealed that the drilled crust, from top to bottom, consists of (1) lava section that is composed of ponded lavas, inflated flows, sheet flows, and massive flows (751 m), (2) lava-dike transition zone (60 m), (3) sheeted dikes (346 m), and (4) gabbroic rocks intruded into screens of contact metamorphosed dikes (Figure 2).

[5] The uppermost crust is made up of a single >74 m-thick ponded lava flow overlain by thin sheet flows. This thick lava correlates with a 32 m-thick massive lava cored in the neighboring pilot Hole 1256C indicating significant basement topography at the time of eruption. By analogy with observations of the modern EPR [*Macdonald et al.*, 1996] and the need for significant topography to pond such a thickness of lava, this massive flow is interpreted to have solidified 5 to 10 km off axis [*Wilson et al.*, 2003]. The lavas directly underlying the ponded flow display rare subvertical hyaloclastite-filled inflation structures, indicative of eruption onto a near horizontal surface [e.g., *Umino et al.*, 2002], and are interpreted to have also solidified off axis. Sheet flows with subordinate massive (>3 m thick) flows make up the bulk of the extrusive section (533.9 to 1004.1 mbsf). Subvertical igneous contacts, commonly brecciated and mineralized, are abundant throughout the sheeted dike complex. The lower ~60 m of the sheeted dikes are strongly recrystallized to microcrystalline granoblastic textures through contact metamorphism by underlying gabbro sills. Secondary mineral assemblages indicate very high geothermal gradients (>1500°C/km) in this region. The plutonic section from 1407 mbsf forms the upper portion of a dike-gabbro transition zone and comprises two gabbroic sills 52 and 24 m thick intruded into a 24 m thick screen of granoblastically recrystallized dikes. The drilled sequence has normal mid-ocean ridge basalt composition and is similar to modern EPR basalts [*Wilson et al.*, 2003, 2006; *Teagle et al.*, 2006]. The gabbroic rocks recovered to date have chemistries similar to the overlying extrusive rocks and sheeted dikes.

[6] The volcanic section in Hole 1256D has an average recovery rate of 37% but this is highly variable and includes several intervals with no recovery (Figure 2). Drilling in massive formations provides higher recovery rates (average ~ 50%) whereas recovery rates in other rock types are typically much lower (Figure 2). The volcanostratigraphy determined on board during ODP Leg 206 and IODP Expeditions 309 and 312 is based on descriptions of the recovered cores, assuming that these are representative of the basement. Although it is acknowledged that this assumption is most probably incorrect, in the absence of other infor-

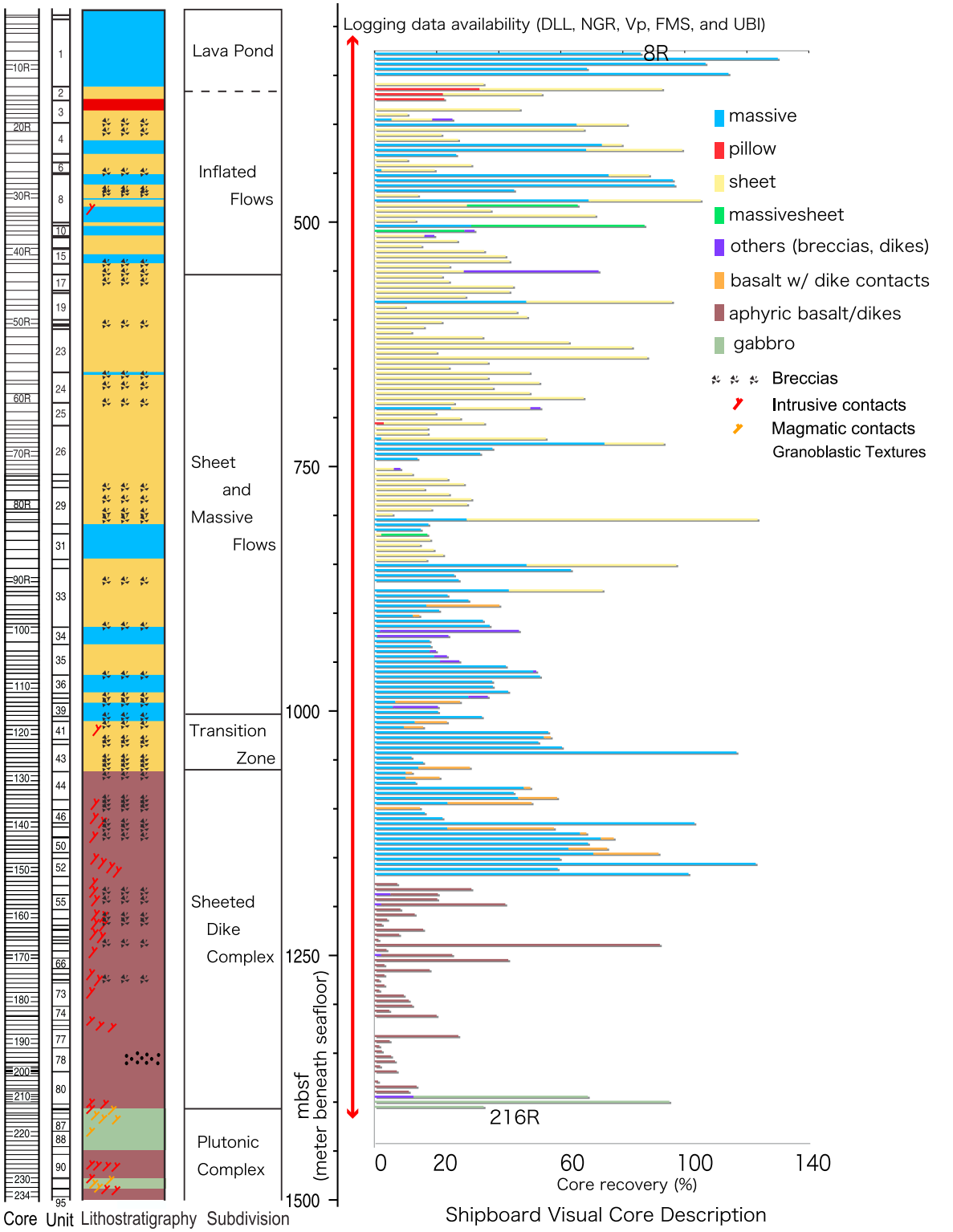
Logging data availability (DLL, NGR, Vp, FMS, and UBI)
8R
216R
massive
pillow
sheet
massivesheet
others (breccias, dikes)
basalt w/ dike contacts
aphyric basalt/dikes
gabbro
Breccias
Intrusive contacts
Magmatic contacts
Granoblastic Textures
Lava Pond
Inflated Flows
Sheet and Massive Flows
Transition Zone
Sheeted Dike Complex
Plutonic Complex
500
750
1000
1250
1500
mbsf (meter beneath seafloor)
0
20
60
100
140
Core recovery (%)
Core
Unit
Lithostratigraphy
Subdivision
Shipboard Visual Core Description

Figure 2

mation, regions of low or no recovery are typically assumed to be similar to the nearest recovered cores.

2.2. Core-Log Integration Studies

[7] There have been relatively few attempts to overcome the inherent biases of the core-derived volcanostratigraphy of ODP basement sites through detailed core-log integration [*Bartetzko et al.*, 2002; *Haggas et al.*, 2001, 2002; *Barr et al.*, 2002; *Révillon et al.*, 2002; *Pockalny and Larson*, 2003; *Bartetzko et al.*, 2001, 2003, 2006]. In these studies, core descriptions and in situ depths were reexamined and lithologic classification criteria developed based on response ranges of the wireline logs and imaging tools. These logging responses were then applied to regions of low and no core recovery to construct a basement stratigraphy. However, these previous studies generally had only limited coverage of the borehole wall due to only single passes by imaging tools, such as the formation microscanner (FMS) and ultrasonic borehole imager (UBI), making it challenging to differentiate, for example, pillow lavas from highly fractured formations. In contrast, multiple passes of Hole 1256D over the three cruises by the FMS and UBI provide greater coverage of the borehole walls. With a more comprehensive data set from Hole 1256D, a more robust lithostratigraphy can be constructed with much greater confidence than earlier studies.

3. Method

3.1. Hole 1256D Logging Operations

[8] Comprehensive wireline logging programs were conducted following drilling on all three cruises, as well as before the initiation of coring on Expedition 309 (Figure 3). All wireline logging data were depth-matched and archived by Borehole Research Group of the Lamont-Doherty Earth Observatory (http://iodp.ldeo.columbia.edu/DATA/IODP/index.html). Single and orthogonal caliper measurements show that the Hole 1256D borehole is in generally good condition with few intervals of significant washout (>14 in.). As such, most of the logging data should be reliable (http://iodp.ldeo.columbia.edu/DATA/). All types of logs are available for the interval from 312 to 1425 mbsf that includes the lower part of the ponded lava down to the uppermost gabbros (Figures 2 and 3).

[9] For simplicity, we hereafter distinguish tools that report a single measurement at each depth as "one-dimensional tools" and instruments that record measurements as a function of depth and direction as "imaging tools. "The former includes the deep and shallow penetration resistivity (Dual LateroLog LLD and LLS), natural gamma ray (NGR), compressional velocity (Vp), density, photoelectric effect factor, and porosity logs. The latter includes: FMS and UBI. Each logging tool measures different in situ physical properties and the responses are dependent on and indicative of the different rock types, structures, and intensity of alteration present in the borehole walls.

[10] NGR, Vp, density, photoelectric effect factor, and porosity were measured with 0.15∼0.20 m sampling intervals. NGR counts are acquired even on relatively irregular borehole walls using the Hostile Environment Natural Gamma Ray Sonde [*Rider*, 1996]. NGR provides a measurement of radioactivity of the formation, in particular that resulting from concentrations of K, U, and Th in the wall rock formation. Total gamma and five-window spectroscopy allows the estimation of individual K, U, and Th concentrations. In ocean floor basalts this tool is most sensitive to the presence of potassium-bearing secondary minerals resulting from the low temperature seawater alteration of basalts [e.g., *Révillon et al.*, 2002]. Vp values are acquired by the Dipole Sonic Imager measuring the sonic wave propagation into the rock formation. Density values are acquired by the Hostile Environment Litho-Density Sonde measuring the electron density of rock formations (that is related to the bulk density). This tool also measures photoelectric effect factor values from the occurrence of photoelectric absorption of the gamma rays in rock formations. Because the pho-

Figure 2. Shipboard summary of Hole 1256D. (left) Lithological subunits determined aboard by shipboard scientists [*Teagle et al.*, 2006]. Sheet flow and sheet-massive flows are distinguished with an arbitrary 3-m cutoff [*Teagle et al.*, 2006]. (right) Cumulative occurrences of rock types. Recovery rate (%) in horizontal axis. Each bar corresponds to a recovered core interval for Core 206-1256D-8R to 312-1256D-216R (312–1425 mbsf) with colored bars proportional to the abundance of the material recovered. According to the different rock types recorded in the shipboard visual core descriptions. Core recovery is plotted for basement depths that were logged, and core recovered below the deepest logged section is not plotted. Note that cores with more than 100% recovery may include unrecovered cores drilled in the previous interval. Thick red line shows the region of downhole tool coverage.

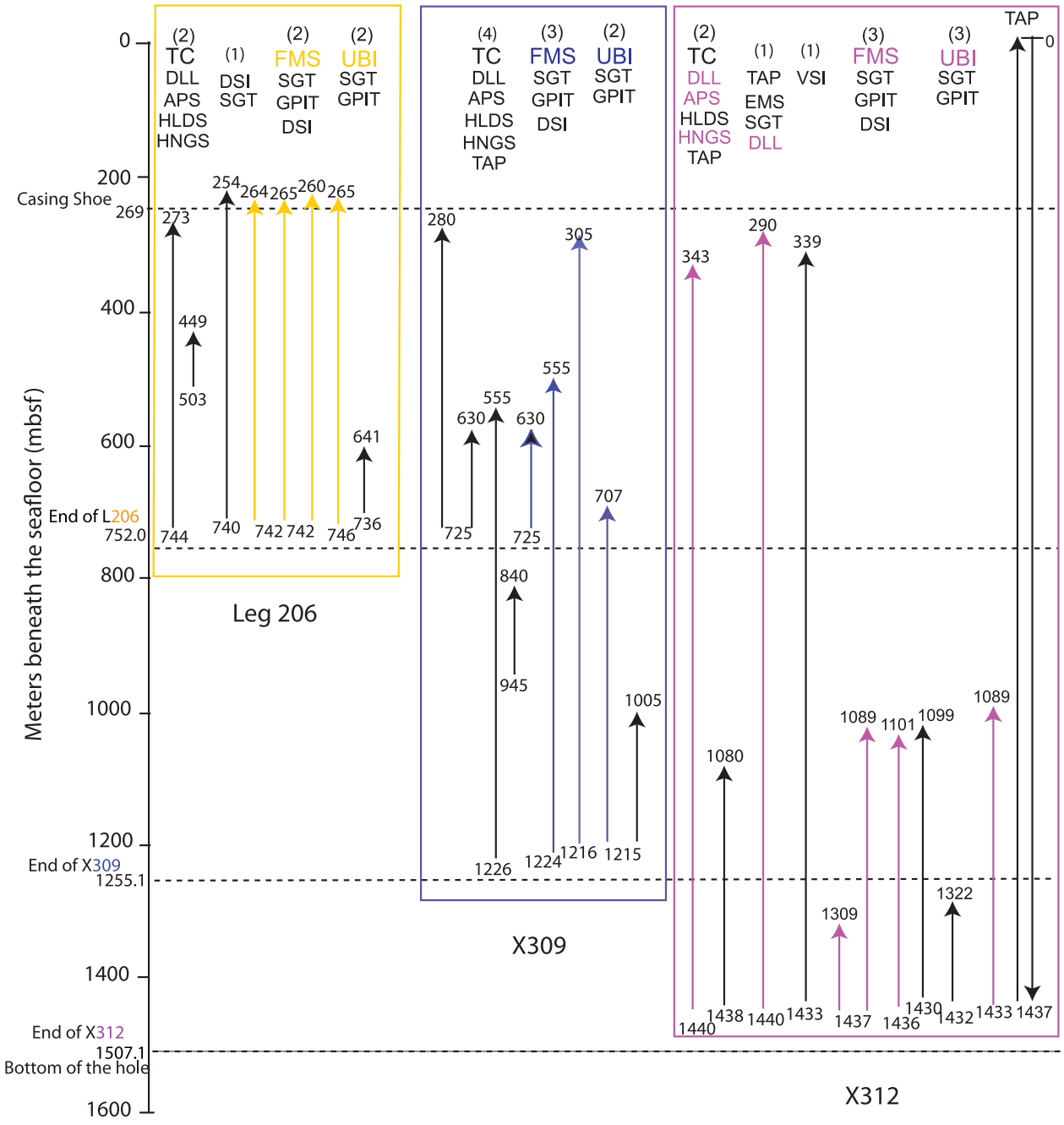

Figure 3. Summary of Leg 206 (yellow), Expedition 309 (blue), and 312 (pink) logging operations. Colored lines and letters indicate wireline logs that were used in this study. The top and bottom of the logging depth was indicated. Numbers in bracket (1∼4) indicate the number of passes with tools indicated below the (number). TC is triple combo, HNGS is hostile environment gamma ray sonde, APS is accelerator porosity sonde, HLDS is hostile environmental lithodensity sonde, DLL is dual laterolog, TAP is temperature acceleration pressure tool, SGT is scintillation gamma ray tool, DSI is dipole sonic imager, GPIT is general purpose inclinometer tool, FMS is formation microscanner, UBI is ultrasonic borehole imager, VSI is versatile seismic imager, and EMS is environmental mechanical sonde.

toelectric effect factor depends on the atomic number of the elements in the formation, these values are used to refer the chemical composition of the rock formations [e.g., *Gardener and Dumanoir*, 1980; *Bartetzko et al.*, 2003]. Porosity values are acquired by the Accelerator Porosity Sonde measuring the energy loss of the emitted neutrons.

[11] LLD, LLS, and FMS measure electric current returns that are sensitive to the porosity structure

and cation exchange capacity of the formation [*Pezard*, 1990]. The electric current from Dual Laterolog tool penetrates ~0.5 m into the wall rock and returns to detectors on the tool strings. The detection range of resistivity by LLD and LLS is from 0.2 to 40,000 ohm m and measurements are carried out typically with 0.15–0.2 m sampling intervals. In contrast, the FMS tool has four orthogonal pads each with 16 sensor buttons that when extended provide partial but significant lateral coverage of the borehole wall (e.g., up to 40% with four orthogonal pads in 8 in. borehole) with high spatial resolution (~0.002 m) resistivity readings. The resulting FMS data provide high-resolution resistivity images of the borehole wall. UBI measures the acoustic reflections from borehole wall with 360° coverage and provides a visualization of the borehole wall reflectivity as two-dimensional images with a sampling resolution of ~0.15 m. Both the FMS and UBI images are azimuthally oriented to the geographic reference frame using the General Purpose Inclinometer Tool. The FMS and UBI in situ physical property measurements essentially provide "scanned images" of the borehole wall that are of great help for determining the morphology of the basement formations penetrated. In Hole 1256D, multiple FMS runs provide significant intervals with nonoverlapping pad traces providing increased lateral coverage of the borehole wall compared to a single pass. The vertical distribution of nonoverlapped pad traces by four, eight, and twelve pads downhole is 35, 45, and 20%, respectively. The multiple passes of the FMS in Hole 1256D result in the FMS logging operation yielding greater than 40 to 60% lateral coverage (as high as 216°) for that over 65% of the logged interval.

[12] The extreme contrast between the highly conductive seawater in the borehole and highly resistive gabbroic rocks led to saturation of the wireline resistivity tools (>4.6 Log ohm/m; e.g., http://www.ldeo.columbia.edu/BRG/ODP/ODP/LEG_SUMM/176/leg176.html). As such the occurrence of gabbroic rocks remains as determined from the core descriptions at the curatorial depth of 1407 mbsf. We await further drilling and logging of Hole 1256D to provide better wireline log data to characterize the plutonic section of Hole 1256D.

3.2. Logging Data Collection

[13] After we closely examined all the wireline logging data from Hole 1256D collected on ODP Leg 206 and IODP Expeditions 309 and 312, we used FMS and UBI images, LLD, LLS, and NGR as primary parameters and density, Vp, photoelectric effect factor, and porosity as secondary parameters to classify rock and flow types in the electrofacies analysis. We found that the combination of the primary wireline log parameters with the FMS images provides the most distinctive signatures for different rock formations. The secondary wireline parameters are useful for detailed chemical composition-rock type determination [e.g., *Bartetzko et al.*, 2003]. However, a preliminary examination of all the wireline data from Hole 1256D indicated that the crust is highly fragmented. Such formations mean that wireline tool responses of these secondary parameters are strongly influenced by the presence of fluid (including hydrogen bounds in altered rocks) or the quality of contact with the borehole wall. Because of these in situ conditions, we have given these secondary parameters less weight in our electrofacies analysis. Instead we have used the resistivity logs as an alternative and more representative recorder of the information provided by the density, Vp, photoelectric effect factor, and porosity data because resistivity is some, albeit unknown function of the local porosity structure and the rock formation [e.g., *Pezard*, 1990].

[14] FMS and UBI images were replotted by using a 2 m window for dynamic calculation onto the depth matched values at the Borehole Research Group, University of Leicester and at the Institute for Frontier Research on Earth Revolution, Japan Agency for Marine-Earth Science and Technology. FMS images can be displayed with either static or dynamic normalization. Static normalization computes the relative contrast in resistivity over the entire logged interval so that absolute values can be comparable downhole. For dynamic normalization, resistivity contrasts are compared within designated short intervals and this approach has been utilized in our analysis because this more strongly emphasizes local contrasts of conductive features. The UBI images are strongly influenced by the hole condition and were mostly utilized to check the locations and appearances of major features on the FMS images.

3.3. Core-Log Correlation and Qualitative Electrofacies Analysis

[15] High-resolution FMS images (.tiff format) were acquired using the GeoFrame™ software and the borehole was subdivided into 50 m intervals for printing onto 36 × 48 inch paper together

with the depth-matched LLD, LLS, NGR, FMS, and caliper logs to enable the "mapping" of the downhole geology. These plotted images when combined with images on GeoFrame were found to be an efficient method of electrofacies analysis as this allowed the complete stratigraphy to be assessed simultaneously and the responses of similar rock types from different intervals to be readily compared.

[16] First, we identified flow boundaries, distinctive conductive fractures, and subvertical contacts using the FMS and UBI images. The lithology of the units between these boundaries was then determined based on the morphologies of the borehole walls as observed from the FMS and UBI images, the ranges of LLD, LLS, and NGR responses, and nature of the recovered core pieces. The FMS caliper measurement was carefully monitored because irregularities in the borehole walls can interfere with resistivity responses.

[17] Next, we investigated the correlation between recovered core pieces and observations on logging interpretation. The preliminary inspection of the FMS images provided us with broad clues to match recovered cores and unrecovered intervals with corresponding rock types. Continuous core pieces are typically only recovered from intervals of homogeneous, slightly altered, massive lavas. We tried to establish the in situ depths of recovered continuous core pieces (approximately >8 cm) by comparing the depths of intervals assumed to be massive flows based on their relatively homogeneous textures on the FMS images with the curatorial depths of continuous core pieces. In some cases, the recovered continuous core pieces can be unambiguously assigned to the depth of the massive lavas observed on FMS images, and then neighboring core pieces can be assigned depths by considering their juxtaposition with respect to the massive lava intervals. One might think that FMS or UBI images may readily be used to relocate brecciated pieces to appropriate fragmented intervals identified. However, the relocation of individual pieces is extremely challenging even when there are distinctive features in cores such as veins and fractures. This is principally due to very low recovery rates in such intervals and the large distance between the exterior of the recovered cores and the borehole walls (>10 cm). We also examined the onboard physical property measurements on the recovered cores (i.e., magnetic susceptibility, gamma ray attenuation porosity, wet bulk density, and natural gamma emission measured by multisensor track) to see how these physical property measurements help us to match core observations to wireline logs. We found that, however, these cores and the measured values represent only limited aspects of the in situ bulk formation because the core recovery rates are so low and recovered core types are strongly biased. Following examination of the complete section, the curatorial depths and the logger's depths were generally found to be no more than a few meters difference in Hole 1256D (Table S1).[1]

[18] Last, we have finalized the classification of lithofacies principally based on wireline logs. These lithofacies classifications are named after rock formation textures on the FMS images. Classifying flow types in a volcanostratigraphy model based on electrofacies analyses relies on criteria that are somewhat different from those for identifications based on observations of surficial lava morphology from underwater vehicles [e.g., *Umino et al.*, 2000]. In electrofacies analyses one observes a cross section of the accumulated lava flows as represented by resistivity contrasts. Following this approach, we can generally identify lava as either as a massive flow, pillow lava, a fragmented interval, or some form of physically altered, fragmented flows.

4. Results

4.1. Hole 1256D Qualitative Volcanostratigraphy

[19] A new igneous stratigraphy of Hole 1256D from 312 to 1425 mbsf is proposed (Figure 4, Table 1) and the characteristic parameters for recognizing each electrofacies are summarized in Table 2. We suggest 10 lithofacies: massive flows, massive off-axis ponded lava, fractured massive flows, thin flows/thick pillows, pillows, fragmented flows, breccias, isolated dikes, dikes in sheeted dike complex, and gabbros.

[20] Massive flows, fractured massive flows, and fragmented flows are the dominant lithofacies in the extrusive sequences and make up approximately 13, 5, and 23%, respectively, of the complete section (Table 3). Pillow lavas make up only 1.4% of our new stratigraphy and are confined to a number of 0.5–3 m thick intervals between 700 and 810 mbsf. The pillow zone between 364 and 388 mbsf identified by shipboard scientists is

[1] Auxiliary materials are available in the HTML. doi:10.1029/2008GC002143.

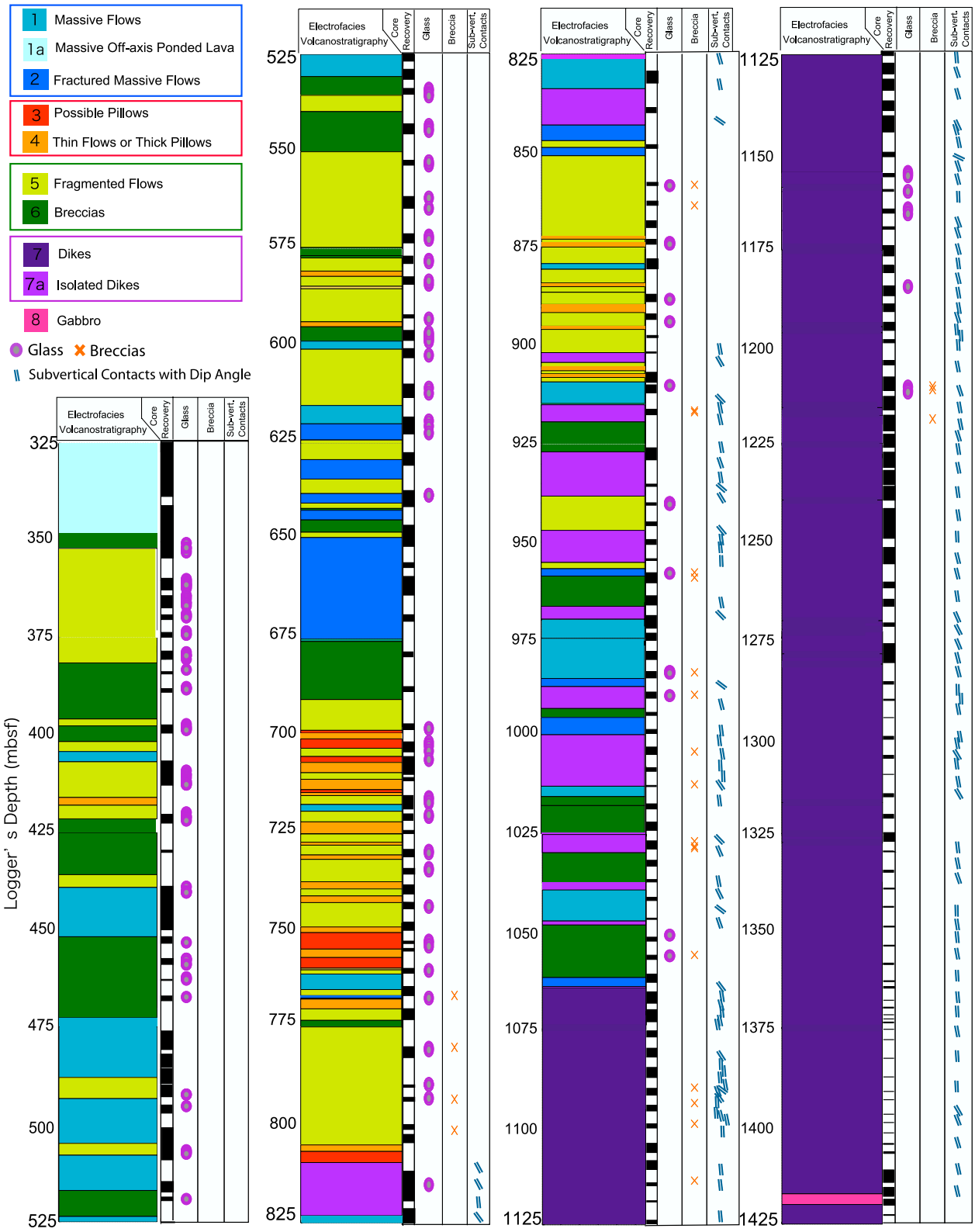
1 Massive Flows
1a Massive Off-axis Ponded Lava
2 Fractured Massive Flows
3 Possible Pillows
4 Thin Flows or Thick Pillows
5 Fragmented Flows
6 Breccias
7 Dikes
7a Isolated Dikes
8 Gabbro
Glass
Breccias
Subvertical Contacts with Dip Angle
Electrofacies Volcanostratigraphy
Core Recovery
Glass
Breccia
Sub-vert. Contacts
Logger's Depth (mbsf)

Figure 4

reinterpreted as a zone of fragmented flows and breccias. Isolated dikes and dikes in sheeted dike complex make 12 and 28% of the new stratigraphy, respectively, and include some brecciated zones with discernible subvertical contacts.

[21] Our new volcanostratigraphy exhibits significant differences in the fractions of breccias and sheet flows compared to the shipboard stratigraphy (Figure 5). This discrepancy clearly indicates that core recovery is highly biased toward better drilled, massive, less fractured rocks.

4.1.1. Massive Flows (1)

[22] We identified massive flows as intervals more than 2 m thick with a homogeneous texture on the FMS and UBI images. These massive flows are mainly located between 430–530 mbsf and 825–1050 mbsf. Irregularly spaced minor fractures with various orientations are common in these flows. LLD and LLS measurements are typically as high as 1.6 ± 0.4 Log-ohm m due to the homogeneous texture and with slightly lower values near fractures. NGR counts are relatively low (4.2 ± 2.3 API; Figure 6 and Table 2).

4.1.2. Massive Off-Axis Ponded Lava (1a)

[23] The massive off-axis ponded lavas that construct the upper ~100 m of basement in Hole 1256D are subdivided from the massive flows. Although their electrofacies characteristics are similar, there are strong geological and geophysical criteria for their recognition as a distinctive subgroup [*Wilson et al.*, 2003] and relatively high core recovery rates give confidence in the shipboard descriptions. LLD and LLS measurements are high 1.9 ± 0.2 Log-ohm m compared to other electrofacies in the extrusive section, indicating low porosity structure. NGR counts are low (2.6 ± 1.3 API), indicating relatively few fractures in this formation (Figure 7 and Table 2).

4.1.3. Fractured Massive Flows (2)

[24] This electrofacies is assigned to flows more than 2 m in thickness with less homogeneous texture than massive flows and commonly rounded fractures apparent on the FMS and UBI images. The thickest fractured massive flow is located from 650 to 675 mbsf. We assume that the fractured massive flows are massive flows that have been physically altered by fracturing or jointing. Owing to the common presence of fractures, LLD and LLS values are slightly lower (1.6 ± 0.3 Log-ohm m) and NGR counts (4.1 ± 2.6 API) are slightly higher than massive flows (Figure 8 and Table 2).

4.1.4. Pillow Lavas (3)

[25] We identified pillow lavas in the FMS and UBI images as rounded bodies with curved rims, radial fractures, downward drooping tear drop shapes, relatively highly conductive interstitial material, and irregular patches within the more massive interiors. The pillow lavas are localized between 700 and 810 mbsf. Lava pillow sizes measured from the FMS images range from a few tens of centimeters to approximately 1 m in diameter. The estimation of lava pillow sizes is limited by the diameter of the borehole which might lead to an underestimation of the percentage of pillows and overestimation the variability in lava flow types. The relatively low LLD and LLS (1.5 ± 0.3 Log-ohm m) and high NGR (5.2 ± 2.2 API) are attributed to the highly fractured, porous structure of the pillow sequence (Figure 9 and Table 2).

4.1.5. Thin Flows/Thick Pillows (4)

[26] We identified thin flows/thick pillows as thin, ~1 m thick flows with relatively homogeneous textures in the FMS and UBI images but common rounded boundaries. The occurrence of this electrofacies is confined to between 410 and 910 mbsf and such rocks are most commonly observed between 575 and 600, 700–810, and 875–910 mbsf. In the interval of 700–801 msbf, these flows appear interbedded with fragmented flows and pillow lavas.

[27] The name of this electrofacies reflects the uncertainty of our determination of this rock type. When the drilling penetrates through the center of a ~1 m thick lava pillow, the wireline log responses it will be similar to that of a ~ 1 m thick flow with

Figure 4. Complete igneous stratigraphy of ODP/IODP Hole 1256D crust. Colored column show the sequence of electrofacies, and these color codes for 10 lithologies are indicated on the left. For simplicity, blue colors summarize the intervals of "massive" textures, red colors summarize pillows or thin flows, green colors indicate fragmented intervals, purple colors indicate dikes, and a pink color indicates gabbros. For volcanostratigraphy, logging depth is used. The columns of black and white stripe show core recovery rates (black indicates recovered) that are shown with using curatorial (drilling) depth. Curatorial depths of recovered glass and breccias, and observed subvertical contacts are shown. Note that the recovered intervals are all pushed up to the top of cored interval.

Table 1. Electrofacies

Top	Bottom	Flow
312.2	348.02	MOPL
348.02	351.98	BR
351.98	353.33	FF
353.33	354.06	FF
354.06	355.37	FF
355.37	358.04	FF
358.04	361.95	FF
361.95	364.44	FF
364.44	369.00	FF
369.00	373.00	FF
373.00	377.00	FF
377.00	381.43	FF
381.43	383.29	BR
383.29	384.64	BR
384.64	386.02	BR
386.02	386.99	BR
386.99	389.00	BR
389.00	389.90	BR
389.90	390.69	BR
390.69	392.24	BR
392.24	393.16	BR
393.16	395.81	BR
395.81	397.58	FF
397.58	399.00	BR
399.00	399.96	BR
399.96	401.60	BR
401.60	402.12	FF
402.12	404.16	FF
404.16	406.78	MAS
406.78	407.75	FF
407.75	409.79	FF
409.79	411.21	FF
411.21	411.99	FF
411.99	413.38	FF
413.38	415.94	FF
415.94	417.93	TP
417.93	421.41	FF
421.41	435.73	BR
435.73	439.00	FF
439.00	451.66	MAS
451.66	456.09	BR
456.09	461.02	BR
461.02	465.06	BR
465.06	466.53	BR
466.53	467.56	BR
467.56	468.20	BR
468.20	471.56	BR
471.56	472.45	BR
472.45	477.72	MAS
477.72	482.96	MAS
482.96	488.00	MAS
488.00	493.43	FF
493.43	503.54	MAS
503.54	504.92	MAS
504.92	506.81	FF
506.81	507.95	FF
507.95	517.00	MAS
517.00	523.66	BR
523.66	524.55	MAS
524.55	530.57	MAS
530.57	535.39	BR
535.39	536.89	FF

Table 1. (continued)

Top	Bottom	Flow
536.89	539.58	FF
539.58	542.31	BR
542.31	543.91	BR
543.91	547.00	BR
547.00	549.88	BR
549.88	554.00	FF
554.00	557.08	FF
557.08	561.39	FF
561.39	564.89	FF
564.87	568.87	FF
568.87	570.78	FF
570.78	574.46	FF
574.46	577.29	BR
577.29	579.52	FF
579.52	580.66	FF
580.66	582.02	TP
582.02	583.29	FF
583.29	584.55	FF
584.55	585.20	TP
585.20	585.56	FF
585.56	585.93	FF
585.93	587.92	FF
587.92	593.67	FF
593.67	594.95	TP
594.95	595.89	BR
595.89	598.62	BR
598.62	600.71	MAS
600.71	604.03	FF
604.03	605.05	FF
605.05	607.93	FF
607.93	609.17	FF
609.17	610.16	FF
610.16	611.46	FF
611.46	612.67	FF
612.67	614.36	FF
614.36	615.15	FF
615.15	617.06	MAS
617.06	617.84	MAS
617.84	619.85	MAS
619.85	620.80	FMAS
620.80	621.36	FMAS
621.36	622.53	FMAS
622.53	623.99	FMAS
623.99	624.92	FF
624.92	625.26	FF
625.26	626.30	FF
626.30	629.00	FF
629.00	632.11	FMAS
632.11	633.99	FMAS
633.99	635.29	FF
635.29	637.72	FF
637.72	638.63	FMAS
638.63	640.16	FMAS
640.16	641.53	FF
641.53	642.00	BR
642.00	644.49	FMAS
644.49	646.70	BR
646.70	647.63	BR
647.63	649.00	FF
649.00	650.74	FMAS
650.74	652.21	FMAS
652.21	653.72	FMAS

Table 1. (continued)

Top	Bottom	Flow
653.72	655.32	FMAS
655.32	655.77	FMAS
655.77	658.13	FMAS
658.13	659.84	FMAS
659.84	664.57	FMAS
664.57	668.47	FMAS
668.47	670.74	FMAS
670.74	671.54	FMAS
671.54	675.60	FMAS
675.60	677.71	BR
677.71	679.61	BR
679.61	682.36	BR
682.36	683.51	BR
683.51	684.72	BR
684.72	686.81	BR
686.81	687.03	BR
687.03	687.48	BR
687.48	689.44	BR
689.44	690.52	BR
690.52	698.42	FF
698.42	699.13	P
699.13	700.61	TP
700.61	703.02	P
703.02	703.73	FF
703.73	704.37	FF
704.37	705.14	FF
705.14	706.66	P
706.66	707.60	TP
707.60	708.28	TP
708.28	709.29	TP
709.29	710.98	FF
710.98	712.60	TP
712.60	713.02	TP
713.02	713.64	TP
713.64	714.38	P
714.38	715.17	TP
715.17	715.36	FF
715.36	715.53	FF
715.53	716.57	FF
716.57	717.45	FF
717.45	718.50	MAS
718.50	719.19	MAS
719.19	720.00	FF
720.00	721.91	FF
721.91	723.12	TP
723.12	724.05	TP
724.05	725.07	TP
725.07	726.56	FF
726.56	727.18	FF
727.18	727.95	TP
727.95	729.31	FF
729.31	730.46	FF
730.46	731.50	TP
731.59	737.33	FF
737.33	737.90	TP
737.90	738.16	TP
738.16	739.17	TP
739.17	739.96	FF
739.96	740.97	FF
740.97	741.85	TP
741.85	742.69	TP
742.69	745.35	FF

Table 1. (continued)

Top	Bottom	Flow
745.35	745.78	FF
745.78	746.64	FF
746.64	747.09	FF
747.09	748.93	FF
748.93	749.45	TP
749.45	750.39	TP
750.39	754.61	P
754.61	755.53	TP
755.53	756.78	TP
756.78	757.20	P
757.20	758.57	P
758.57	759.51	P
759.51	759.96	TP
759.96	761.02	FF
761.02	762.14	MAS
762.14	763.76	MAS
763.76	765.00	MAS
765.00	765.27	FF
765.27	766.55	FF
766.55	767.18	TP
767.18	767.45	FF
767.45	769.38	TP
769.38	769.96	TP
769.96	770.60	FF
770.60	771.00	FF
771.00	772.04	FF
772.04	772.46	FF
772.46	772.92	FF
772.92	774.76	BR
774.76	775.16	FF
775.16	776.67	FF
776.67	778.29	FF
778.29	780.84	FF
780.84	781.37	FF
781.37	783.04	FF
783.04	784.09	FF
784.09	785.10	FF
785.10	786.47	FF
786.47	790.67	FF
790.67	795.04	FF
795.05	796.11	FF
796.11	797.12	FF
797.12	800.29	FF
800.29	801.96	FF
801.96	802.71	FF
802.71	805.05	FF
805.05	806.73	TP
806.73	809.58	P
809.58	815.95	MAS
815.95	817.51	ID
817.51	823.21	ID
823.21	823.52	ID
823.52	826.17	ID
826.17	828.26	MAS
828.26	829.11	MAS
829.11	833.90	MAS
833.90	843.23	ID
843.23	845.86	FMAS
845.86	847.23	FMAS
847.23	847.66	FF
847.66	848.07	FF
847.66	848.98	FF

Table 1. (continued)

Top	Bottom	Flow
971.54	975.68	MAS
975.68	979.24	MAS
979.24	981.72	MAS
981.72	983.57	MAS
983.57	985.26	MAS
985.26	985.77	FMAS
985.77	986.50	FMAS
986.50	987.33	FMAS
987.33	992.96	ID
992.96	995.25	BR
995.25	996.36	FMAS
996.36	999.15	FMAS
999.15	999.69	FMAS
999.69	1002.66	ID
1002.66	1004.67	ID
1004.67	1007.96	ID
1007.96	1011.68	ID
1011.68	1017.84	ID
1017.84	1027.85	ID
1027.85	1029.39	ID
1029.39	1031.70	BR
1031.70	1033.82	BR
1033.82	1034.44	BR
1034.44	1036.16	BR
1036.16	1037.08	BR
1037.08	1038.10	MAS
1038.10	1038.91	MAS
1038.91	1045.25	ID
1045.25	1046.88	ID
1046.88	1047.91	ID
1047.91	1058.07	BR
1058.07	1061.37	BR
1061.37	0163.71	FMAS
1063.71	1066.15	VD
1066.15	1067.83	VD
1067.83	1072.82	VD
1072.82	1073.22	VD
1073.22	1073.55	VD
1073.55	1080.08	VD
1080.08	1080.33	VD
1080.33	1085.56	VD
1080.56	1085.68	VD
1085.68	1089.29	VD
1089.29	1091.63	VD
1091.63	1093.35	VD
1093.35	1093.99	VD
1093.99	1094.94	VD
1094.94	1098.10	VD
1098.10	1104.44	VD
1104.44	1106.90	VD
1106.90	1112.72	VD
1112.72	1115.55	VD
1115.55	1118.76	VD
1118.76	1123.94	VD
1123.94	1125.84	VD
1125.84	1130.87	VD
1130.87	1136.36	VD
1136.36	1140.25	VD
1140.25	1143.19	VD
1143.19	1147.00	VD
1147.00	1155.14	VD
1155.14	1158.97	VD

Table 1. (continued)

Top	Bottom	Flow
848.98	850.46	FMAS
850.46	851.09	FMAS
851.09	857.67	FF
857.67	859.68	FF
859.68	860.70	FF
860.70	862.07	FF
862.07	865.18	FF
865.18	869.23	FF
869.23	871.75	FF
871.75	872.48	TP
872.48	873.32	FF
873.32	874.50	TP
874.50	878.64	FF
878.64	880.11	MAS
880.11	883.61	FF
883.61	884.56	TP
884.56	885.98	FF
885.98	886.00	TP
886.00	889.11	FF
889.11	890.09	TP
890.09	891.20	TP
891.20	894.68	FF
894.68	895.53	TP
895.53	899.22	FF
899.22	901.47	FF
901.47	904.01	ID
904.01	905.11	FF
905.11	906.11	TP
906.11	906.89	FF
906.89	907.84	TP
907.84	908.99	FF
908.99	910.85	MAS
910.85	912.40	MAS
912.40	914.51	MAS
914.51	914.84	BR
914.84	919.23	ID
919.23	920.68	ID
920.68	922.63	BR
922.63	923.54	BR
923.54	926.88	BR
926.88	930.37	ID
930.37	931.87	ID
931.87	935.68	ID
935.68	938.22	ID
938.22	938.82	FF
938.82	943.93	FF
943.93	944.80	FF
944.80	945.19	FF
945.19	945.75	FF
945.75	947.00	FF
947.00	949.79	ID
949.79	951.77	ID
951.77	955.22	ID
955.22	956.82	FF
956.82	957.81	FMAS
957.81	958.71	FMAS
958.71	961.03	BR
961.03	962.09	BR
962.09	964.25	BR
964.25	966.46	BR
966.46	969.77	ID
969.77	971.54	MAS

Table 1. (continued)

Top	Bottom	Flow
1158.97	1160.94	VD
1160.94	1163.62	VD
1163.62	1170.13	VD
1170.13	1173.03	VD
1173.03	1176.23	VD
1176.23	1178.98	VD
1178.98	1181.25	VD
1181.25	1186.00	VD
1186.00	1188.45	VD
1188.45	1194.65	VD
1194.65	1196.17	VD
1186.17	1201.26	VD
1201.26	1208.41	VD
1208.41	1215.39	VD
1215.39	1217.49	VD
1217.49	1219.63	VD
1219.63	1223.38	VD
1223.38	1227.80	VD
1227.80	1235.32	VD
1235.32	1239.44	VD
1239.44	1243.28	VD
1243.28	1250.67	VD
1250.67	1256.77	VD
1256.77	1261.44	VD
1261.44	1266.40	VD
1266.40	1270.39	VD
1270.39	1272.63	VD
1272.63	1278.45	VD
1278.45	1281.11	VD
1281.11	1282.64	VD
1282.64	1285.52	VD
1285.52	1288.66	VD
1288.66	1298.56	VD
1298.56	1301.10	VD
1301.10	1305.47	VD
1305.47	1308.82	VD
1308.82	1314.02	VD
1314.02	1316.58	VD
1316.58	1327.06	VD
1327.06	1329.71	VD
1329.71	1332.38	VD
1332.38	1342.41	VD
1342.41	1347.63	VD
1347.63	1353.46	VD
1353.46	1357.13	VD
1357.13	1360.78	VD
1360.78	1365.09	VD
1365.09	1369.51	VD
1369.51	1371.00	VD
1371.00	1375.54	VD
1375.54	1379.15	VD
1379.15	1382.00	VD
1382.00	1390.11	VD
1391.00	1393.00	VD
1393.00	1398.69	VD
1398.69	1409.44	VD
1409.44	1410.94	VD
1411.00	1417.25	VD
1417.25	1419.99	VD
1419.99	1423.00	VD
1423.00	1425.00	VD

distinctive flow boundaries on the top and bottom, because the curved rims of the pillow may not be intersected by the borehole or apparent on the FMS images. Hence, it is difficult to unequivocally determine solely from wireline logs whether this lithofacies type represents sheet flow or relatively thick pillow lava. LLD and LLS measurements are typically higher than the immediately overlying or underlying intervals (1.6 ± 0.4 Log-ohm m). NGR counts are on average moderate but display a wide range (4.6 ± 2.4 API; Figure 9 and Table 2).

4.1.6. Fragmented Flows (5)

[28] Fragmented flows are intervals with common fractures that appear as diagonal mesh-like textures on the FMS and UBI images. Fragmented flows are the most abundant electrofacies in the volcanic sequence of Hole 1256D. These flows are located throughout the volcanic section of the hole from 350 to 1064 mbsf and thickness of individual units varies from a few tens of centimeters to >20 m (e.g., intervals 351–381 and 775–805 mbsf). On the FMS and UBI images, we observe thick intervals displaying the mesh fabric morphology, isolated by highly conductive, flow boundary zones or fractures. We suspect that the fragmented flows originate from massive flows although pervasive fracturing makes it difficult to discount other origins. A few intervals of fragmented flows correspond to recovered samples of breccia. Identifying exact in situ locations of those breccia pieces is challenging because there are multiple high resistivity patches among fragmented, conductive formation on the FMS and UBI images, any of which could be the original sites. LLD and LLS measurements are moderate (1.5 ± 0.4 Log-ohm m) and NGR is relatively high (4.7 ± 2.4 API; Figure 7 and Table 2).

4.1.7. Breccias (6)

[29] We identified breccias as intervals with completely fragmented textures on the FMS and UBI images, in which the fragments of the original formations appear to be chaotically arranged. The highly fragmented texture of these formations makes it difficult to distinguish lithologic boundaries and conductive fractures. This electrofacies is associated with low LLD and LLS (1.5 ± 0.4 Log-ohm m) and high NGR (4.4 ± 2.4 API) compared to adjacent formations (Figures 7 and 8 and Table 2). Breccias are most common in the upper (350–700 mbsf) and lower (910–1060 mbsf) portions of the volcanic sequence.

Table 2. Parameters in Each Lithofacies for Qualitative Volcanostratigraphy[a]

Lithofacies	Primary Parameters			FMS/UBI Criteria	Secondary Parameters			
	LogLLD	LogLLS	NGR		Den.	Poro.	Vp	PEF
1 Massive flows	2.0 ± 0.3	2.0 ± 0.3	2.6 ± 0.8	>2 m thick, with almost no developed fractures resulting in featureless, homogeneous textures.	2.9 ± 0.3	8.5 ± 5.8	5.7 ± 0.4	3.9 ± 1.0
1a Massive off-axis ponded lava	1.9 ± 0.2	1.7 ± 0.2	2.6 ± 1.3	Homogeneous texture, subordinate fractures.	2.9 ± 0.6	6.7 ± 1.8	5.7 ± 0.3	4.5 ± 0.7
2 Fractured massive flows	1.6 ± 0.2	1.6 ± 0.2	3.8 ± 1.3	Less homogeneous texture due to some fracture development, >2 m thick.	2.8 ± 0.2	12.3 ± 6.0	5.4 ± 0.4	3.7 ± 0.7
3 Pillow lavas	1.6 ± 0.2	1.5 ± 0.2	4.4 ± 1.1	An oval to subround outline with radial fracture inside, associated with altered interpillow materials showing high conductivity.	2.8 ± 0.3	16.4 ± 6.9	5.2 ± 0.3	3.3 ± 0.8
4 Thin flows or thick pillows	1.6 ± 0.2	1.6 ± 0.2	4.3 ± 1.3	Similar to homogeneous texture in massive flows disturbed by distinctive flow boundaries or horizontal fractures, <2 m thick.	2.7 ± 0.3	17.2 ± 9.2	5.2 ± 0.4	3.3 ± 0.9
5 Fragmented flows	1.4 ± 0.3	1.4 ± 0.3	5.7 ± 2.8	Brecciated and develop meshy fractures but individual blocks are only slightly displaced each other, thickness vary.	2.6 ± 0.3	24.8 ± 13.3	4.9 ± 0.5	2.8 ± 0.8
6 Breccias	1.2 ± 0.3	1.0 ± 0.3	4.9 ± 2.0	Completely fragmented, no morphology preservation, the mixture of extremely fine high and low FMS conductivity patches.	2.5 ± 0.4	37.7 ± 23.1	4.8 ± 0.8	2.6 ± 0.8
7a Isolated dikes	1.8 ± 0.3	1.6 ± 0.4	2.3 ± 1.0	Distinguished by highly conductive, steep dip fractures, most likely representing intrusive contacts against the host extrusive rocks.	2.6 ± 0.4	20.2 ± 18.7	5.6 ± 0.4	2.8 ± 1.1
7 Dikes	2.6 ± 0.6	2.3 ± 0.4	4.3 ± 1.3	Recognized by subparallel, subvertical fractures spaced ~ 0.6 m apart, indicating dike contacts.	2.9 ± 0.1	7.3 ± 4.3	5.8 ± 0.3	2.9 ± 0.2
8 Gabbro	NaN	NaN	2.8 ± 0.4	data only available from cores	2.9 ± 0.0	2.9 ± 0.4	6.5 ± 0.1	2.9 ± 0.0

[a] Units are LogLLD and LogLLS in ohm m, NGR in API counts, den (density) = g/cm^3, poro (porosity) = %, Vp (compressional velocity) = m/s, PEF (photoelectric factor) = barns/e$^-$. Note that both primary and secondary parameters are calculated from wire-line log during Expedition 312 (see Figure 3).

Table 3. Summary of the New Volcanostratigraphy Model[a]

Lithology	Whole Hole %	Volcanic Section %
Massive flows	10.29	14.3
Ponded lava	3.23	4.5
Fractured massive flows	5.17	7.2
Fragmented flows	23.11	32.1
Thin flows or thick pillows	3.42	4.8
Pillows	1.36	1.9
Breccias	13.26	18.6
Dikes in dike complex	28.01	
Isolated dikes	11.93	16.6
Gabbros	0.25	

[a] Proportion of each lithofacies with respect to entire examined depth 325–1425 mbsf (left) and to only volcanic section (325–1064 mbsf).

[30] Breccia intervals in this lower zone correspond to the common breccia samples recovered around the lithologic transition zone between 1000 and 1060 mbsf. We presume that these breccias were rubble formed by collapse of inflated lobate sheet flows or talus rubble in tension fissures and faults. Some breccia zones occur along subvertical contacts that may be dike margins (e.g., at 914 mbsf).

4.1.8. Dikes in Sheeted Dike Complex (7)

[31] We identified the Dikes in sheeted dike complex (7) that comprise the ~ 350 m of the Hole 1256D sheeted dike complex (1064–1412 mbsf). We identified fractures that are separated by subparallel, subvertical, high-conductivity contacts with consistent orientations as individual dike margins. These features indicate the presence of a sheeted dike complex (Figures 8 and 10). Eighty-six subvertical contacts were identified in the logs between 1064 and 1412 mbsf. Assuming individual dike thickness is measured between a pair of chilled contacts, the average thickness of dikes is 0.5 ± 0.8 m. The average dip and dip direction of the contacts are ~79° ± 8° and 053 ± 23, respectively, calculated by using statistics of spherical

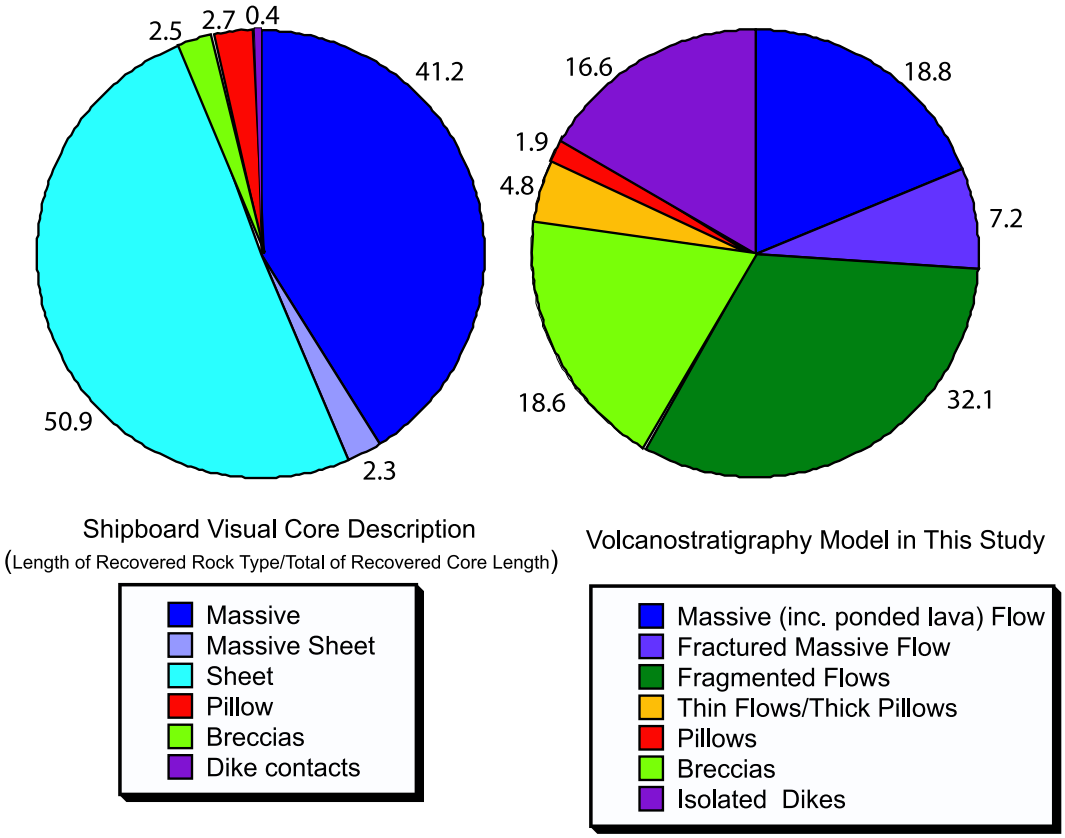

Figure 5. Comparison of rock types in the volcanic section suggested between the (left) shipboard and (right) electrofacies-based igneous stratigraphy. The fraction of each rock type in the shipboard lithostratigraphy was derived from visual core descriptions from Leg 206, Expedition 309 and 312 by calculating a total of recovered core length of a rock type divided by a total of recovered core length. The fraction of each rock type in the electrofacies-based stratigraphy is also shown in Table 3.

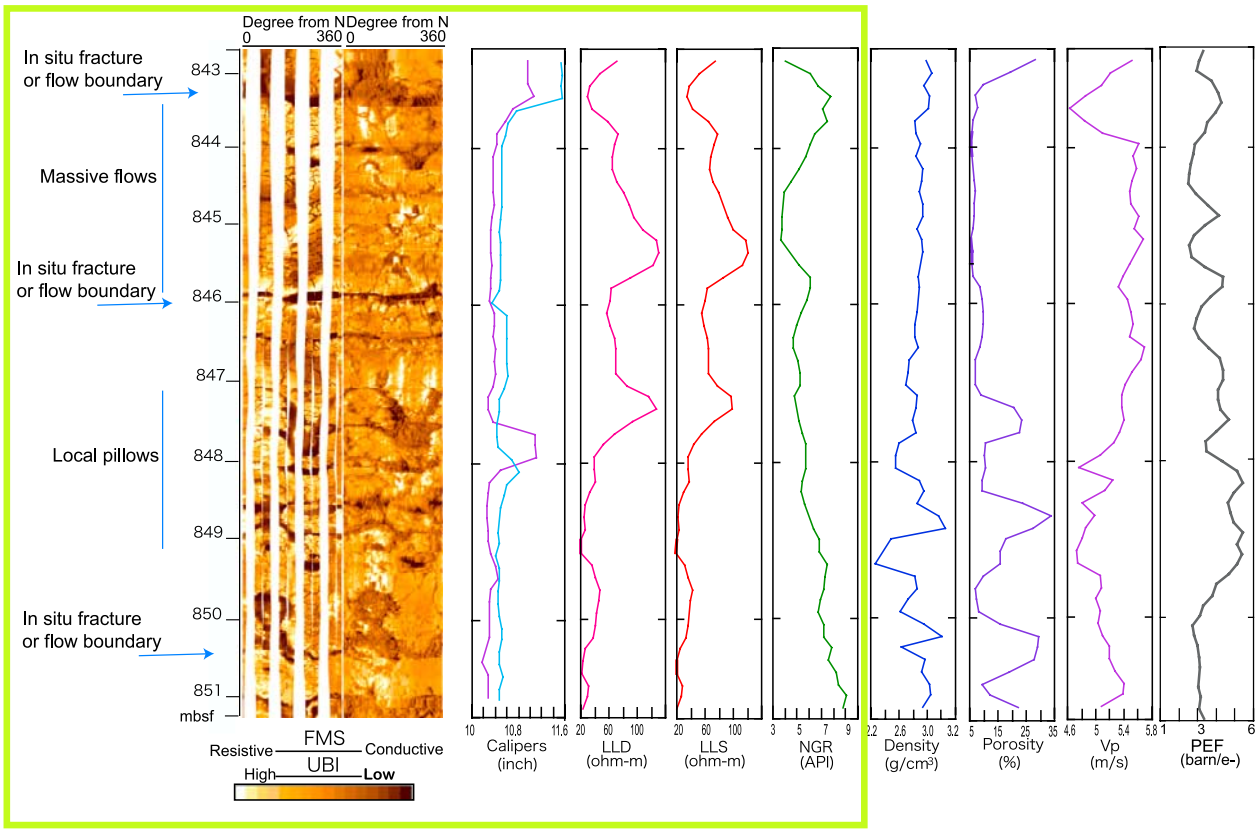

Figure 6. Example of electrofacies analyses over the interval 842–852 mbsf showing in situ fractures or flow boundaries. These boundaries are listed as lithological boundaries in Table S1. FMS and UBI sampling interval were 0.002 and 0.15 m, respectively, and the plot is derived from a dynamically processed 2 m window in GeoFrame. PEF is photoelectric effect factor.

coordinate system [*Fisher et al.*, 1987] (Figures 11a and 11b). This is in good agreement with dike margin measurements made on the cores recovered from this interval (average dip 76° ± 16° (N = 19), see structure_log and dike_log in the work of *Teagle et al.* [2006]). The dike orientation suggests that the sheeted dike complex at Site 1256 crust is tilted slightly away from the paleospreading ridge. The FMS and UBI textures of the dikes are similar to those of the massive flows although dikes are commonly brecciated along subvertical contacts. LLD and LLS values increase dramatically below 1064 mbsf to 2.6 ± 0.6 (Log-ohm m), which is 10 times higher than that of upper volcanic flows, indicative of the paucity of fractures in this formation except the subvertical contact zones. NGR values are relatively high on average (4.3 ± 1.3 API) probably due to strong alteration and mineralization along the subvertical contacts as evidenced in the recovered cores. The values of LLD and LLS are generally high (>3.0 Log-ohm m) in the dike complex. Localized, anomalously high LLD readings (∼ 4.0 Log-ohm m) at 1345 mbsf coincide with the first downhole occurrence of granoblastic dikes (Table 2). Subhorizontal to moderate dipping, evenly spaced (0.1∼1 m) linear features are observed in the cores of dikes (localized around 1119–1124, 1137–1143, 1147–1155, 1226–1227, 1236–1240, 1244–1251, 1258–1261, 1263–1266, 1274–1277, 1279–1295, 1310–1329, 1333–1338, 1343–1345, 1350–1369, 1371–1376, 1383–1409 mbsf) but the origin of these features remains unknown. These features may be open fractures or cooling joints orthogonal to dike margins.

4.1.9. Isolated Dikes (7a)

[32] We identified isolated dikes within the volcanic section (<1064 mbsf) which exhibit massive flow-like textures on the FMS and UBI images sandwiched between pairs of subvertical contacts with attitudes of dips similar to margins observed in the underlying sheeted dike complex (Figure 8). These isolated dikes observed from the FMS images are reminiscent of the narrow interfingered

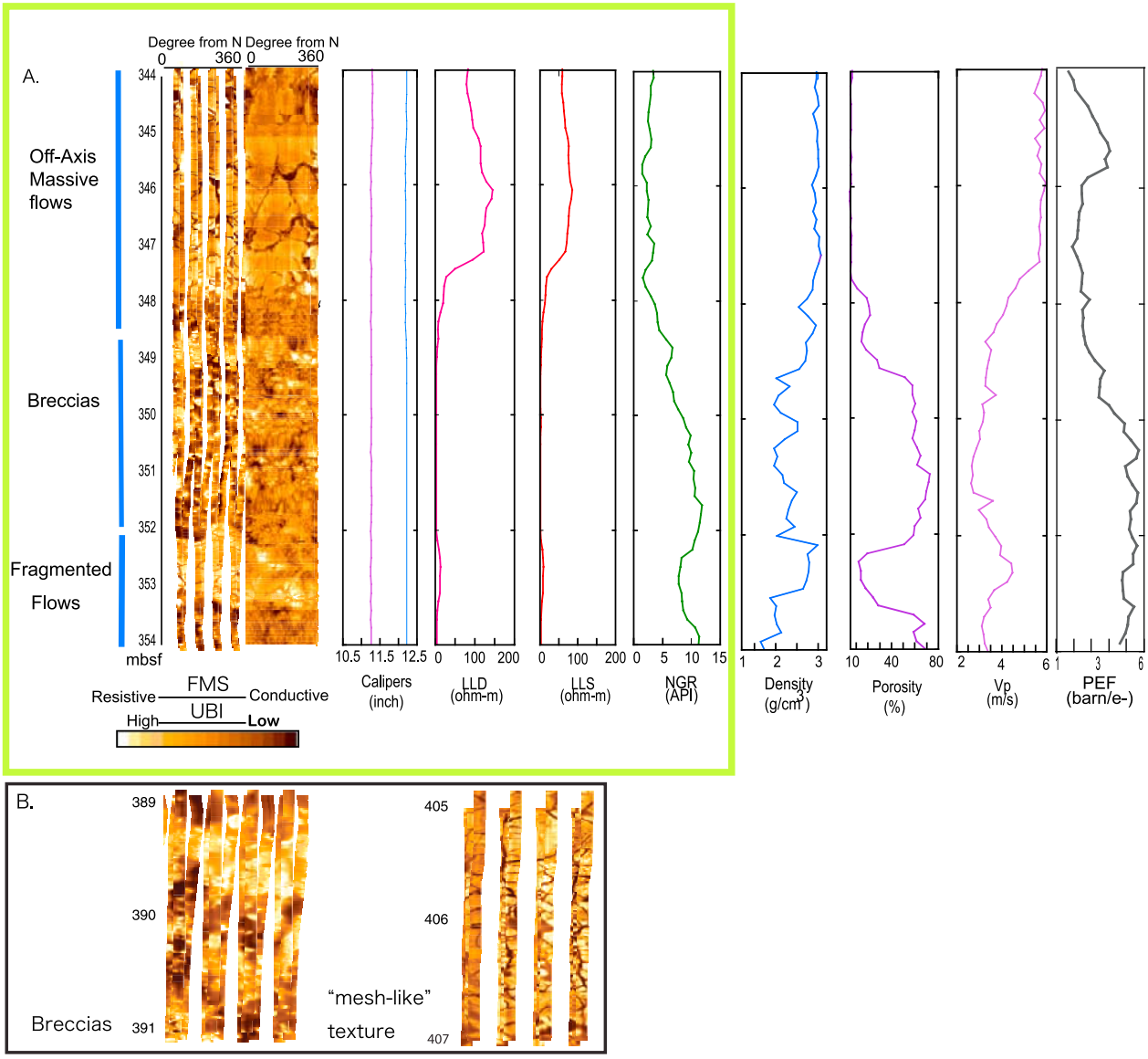

Figure 7. (a) Example of electrofacies analyses over the interval 344–354 mbsf showing the base of the massive off-axis ponded lava flow underlain by breccias and fragmented flows. Yellow box indicates the main parameters used for the analysis of this section (see detail in text). (b) Magnified version of (left) "mesh-like" texture and (right) brecciation.

dikes rarely present in the recovered cores although it is difficult to validate one-to-one correlations (e.g., interfingered dikes in Core 309-1256D-120R-1, 8–26 cm and Isolated Dikes observed at 1018 mbsf on the FMS image). We found 28 Isolated Dikes between 810 and 1064 mbsf with average thickness of 0.5 ± 1.8 m (Figures 11a and 11b). The average dip and dip directions of the contacts are ~79° ± 23° and 033 ± 67, respectively, calculated by using statistics of spherical coordinate system [*Fisher et al.*, 1987]. LLD and LLS values are slightly higher than that of massive flows (1.7 ± 0.4 (Log-ohm m)) and NGR is low to moderate (3.6 ± 2.9 API) (Table 2). Below

Figure 8. Electrofacies analyses over the interval 1025–1125 mbsf with FMS, UBI, LLD and LLS, and NGR wireline logs. Black and blue sinusoid lines indicate subvertical contacts of isolated dikes and dikes in dike complex, respectively. The red line and arrow indicate the boundary between lowermost fragmented flow and massive flow intervals indicating the bottom of the transition zone. The range of LLD and LLS increases drastically from the upper to lower part of the dike interval due to decreasing porosity in the formation.

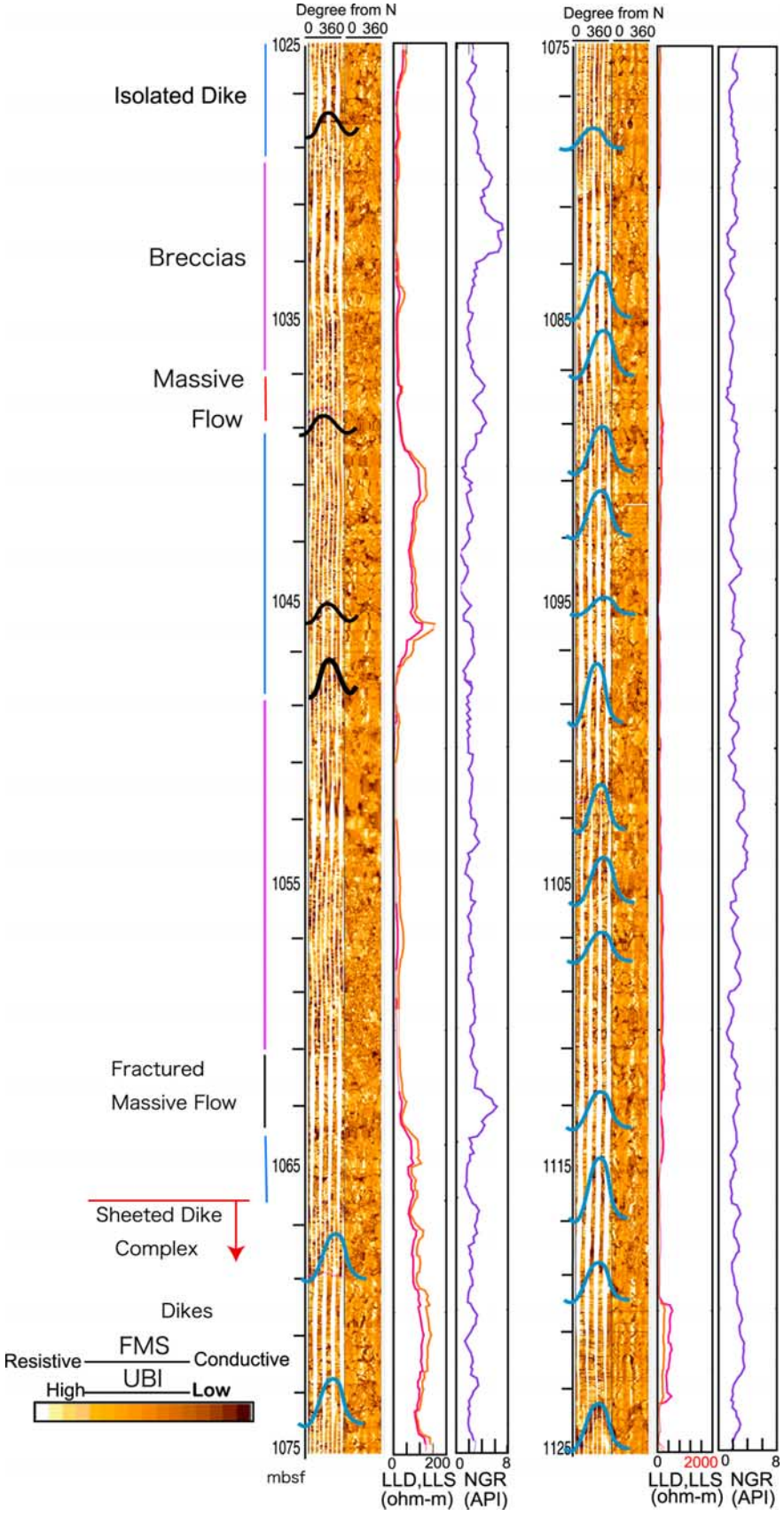
Degree from N
0 360 0 360
Isolated Dike
Breccias
Massive
Flow
Fractured
Massive Flow
Sheeted Dike
Complex
Dikes
FMS
Resistive
Conductive
UBI
High
Low
1025
1035
1045
1055
1065
1075
mbsf
0 200 0 8
LLD,LLS NGR
(ohm-m) (API)
1075
1085
1095
1105
1115
1125
0 2000 0 8
LLD,LLS NGR
(ohm-m) (API)

Figure 8

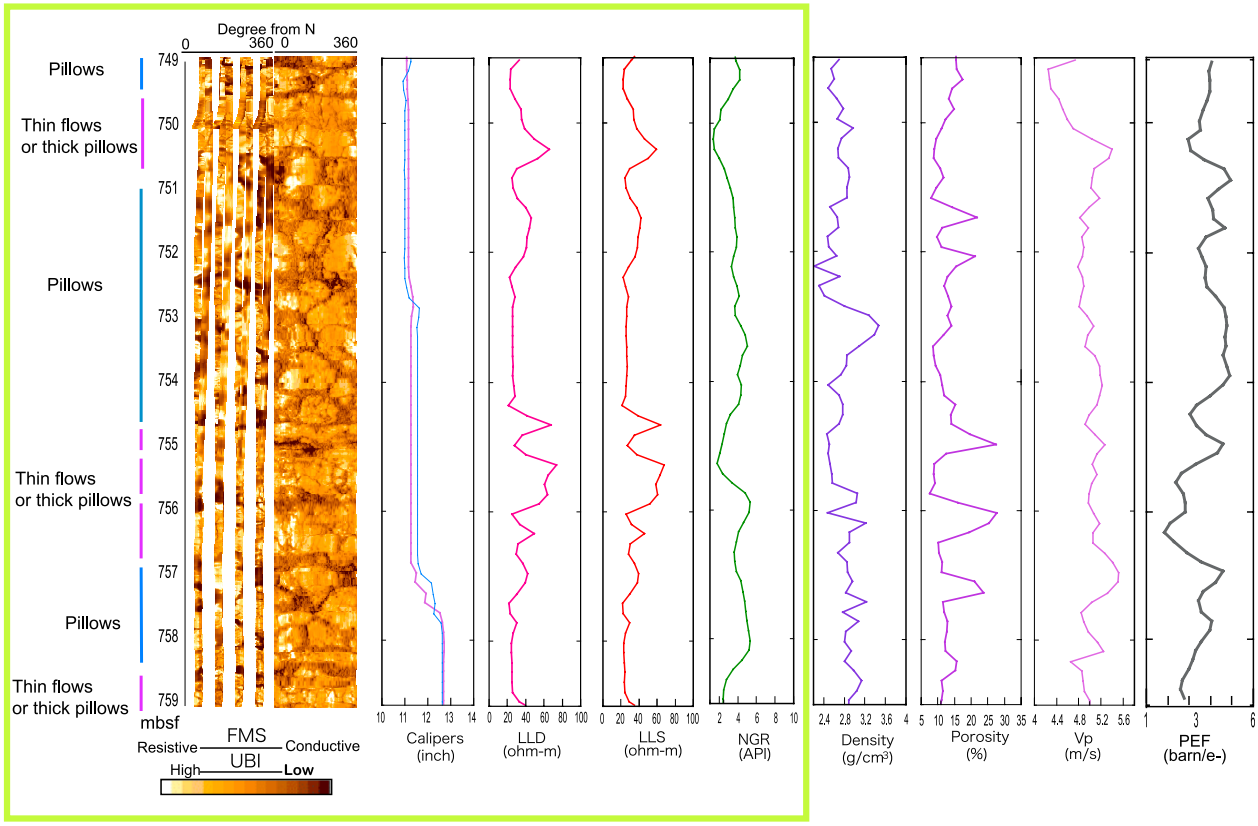

Figure 9. Electrofacies analyses over the interval 749–759 mbsf in which possible pillow lavas were observed. Particularly in 751–755 mbsf, curved rims, radiation fractures, highly altered patches, and highly conductive (darker color in this image) interpillows are clearly observed. 755–757 mbsf, two 1 m flows with distinctive flow boundaries are observed, both of which we interpreted as thin flows or thick pillows.

910 mbsf in the lithologic transition zone, isolated dikes are commonly associated with brecciated margins.

4.1.10. Gabbros (8)

[33] As discussed previously, the malfunction of the resistivity sensors due to the extreme contrast between highly conductive seawater filling the borehole and highly resistive igneous formation precludes detailed analysis of this section. Gabbros are assigned to our new crustal stratigraphy using the curatorial depths from the recovered core (Figure 10).

5. Discussion

5.1. Pillows or Not Pillows

[34] In previous core-log integration studies, to obtain characteristic logging tool responses for a rock type, comparisons were made among the rock type from core observations, logging tool responses, and a partial cross-sectional view of the accumulated lava flows as represented by resistivity contrasts on the FMS images. The obtained logging responses become criteria to determine rock types particularly in zones of low and no core recovery [e.g., *Bartetzko et al.*, 2002; *Révillon et al.*, 2002; *Barr et al.*, 2002]. Following this approach, however, we found that the identification of pillow lavas is particularly challenging for two reasons. First, pillows can be misidentified in core observations. The traditional pillow determination criteria in recovered core pieces are based on pillows seen in ophiolites [e.g., *Gillis and Sapp*, 1997], such as (1) curved or rounded chilled margins with radial fracturing, (2) changes in grain size from the rim to the center of pillows and the presence of glass and varioles. Although helpful, these criteria are not definitive for identifying pillow lavas in drilled cores. Second, the challenge in core-log integration is to interpret and subdivide the overlapping ranges of tool responses to establish a representative set of responses for pillows. It is obvious from our FMS images that curved margins of pillows and fractured pillow interiors

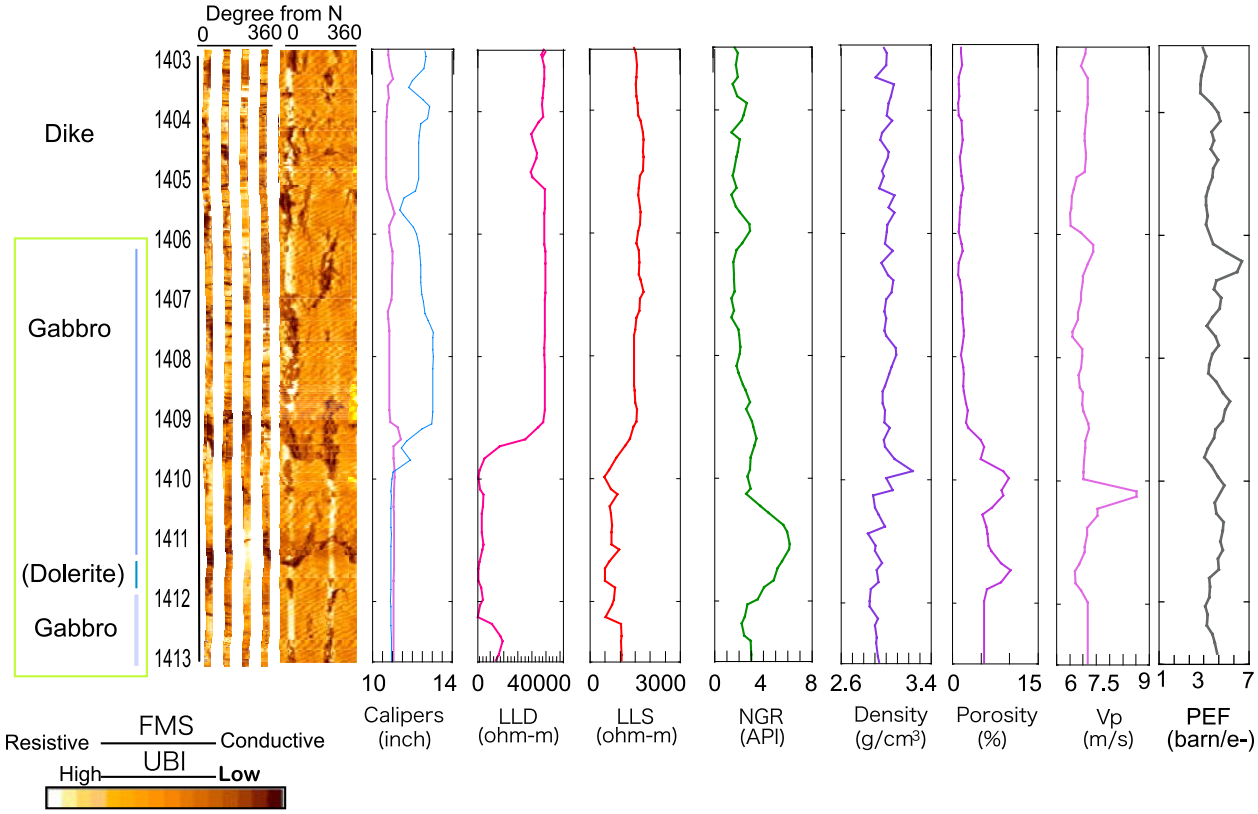

Figure 10. Electrofacies analyses over the interval 1403–1413 mbsf where IODP Expedition 312 recovered gabbroic rocks. We locate the depth of the gabbro based on the curatorial depths because DualLaterolog tool appears to have reached its detection limit (see LLD values). This may be due to the inappropriate preparation of the borehole prior to logging, resulted in a more than 5 times resistivity contrast between the borehole wall and water-filled borehole. Before future logging of gabbroic intervals the borehole should be flushed with fresh water to reduce the resistivity contrast (http://www.ldeo.columbia.edu/BRG/ODP/ODP/LEG_SUMM/176/leg176.html).

resemble characteristics of fragmented flow formations, making it difficult to use logging tool responses to isolate a rock type (e.g., fragmented flow) from others (e.g., pillows). For our analysis, developing methods to confidently identify lava morphologies from wireline logs, specifically from the FMS images, was necessary.

[35] To explore if a correlation between recovered core pieces and pillow-like FMS images is available, we revisited the distribution of the cores recovered and FMS images from two other ODP/IODP holes. We first visited IODP Hole U1301B that drilled into intermediate spreading rate crust on the eastern flank of the Juan de Fuca Ridge, from which many apparent pillow lavas were recovered [*Fisher et al.*, 2005]. However, a paucity of good FMS logs precludes similar analysis. Future drilling and logging at this site may provide sufficient FMS borehole coverage to test pillow lava identification and occurrences.

[36] We next examined ODP Hole 801C, which penetrated into ocean crust formed at a fast spreading rate [*Plank et al.*, 2000]. At this site, the previous most comprehensive core-log integration study was carried out [*Barr et al.*, 2002]. Their pillows were "characterized by more variable log responses. . .the average log values are intermediate between those for massive basalts and breccia. . .FMS images of pillow lavas are characterized by bright, rounded regions of relatively uniform resistivity (pillows) separated by darker, more conductive intervals that represent altered interpillow zones. "However, our examination of the visual core descriptions from Hole 801C [*Plank et al.*, 2000] and comparison with the shipboard lithostratigraphy and FMS images as reported by *Barr et al.* [2002] suggest that their core-log integration overestimated pillows and the aforementioned set of log responses for pillows may be erroneous. *Barr et al.* [2002] cite the presence of curved chilled margins as a distinguishing characteristic of pillows in the shipboard core lithostra-

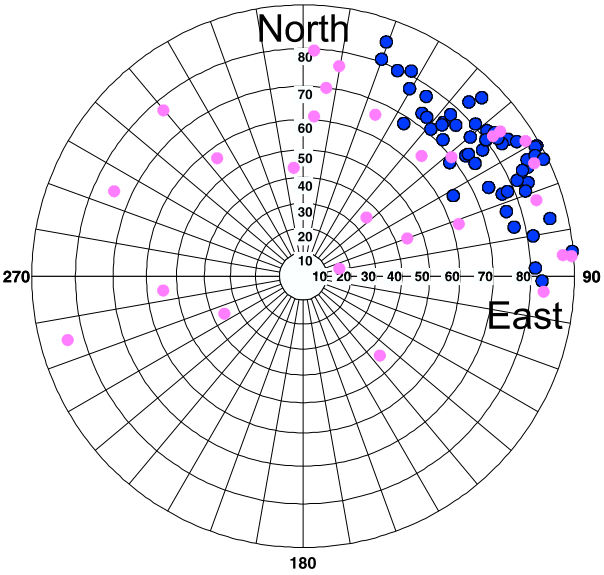

Dips and Dip Direction of Dikes in dike complex
Dips and Dip Direction of Isolated Dikes

A.

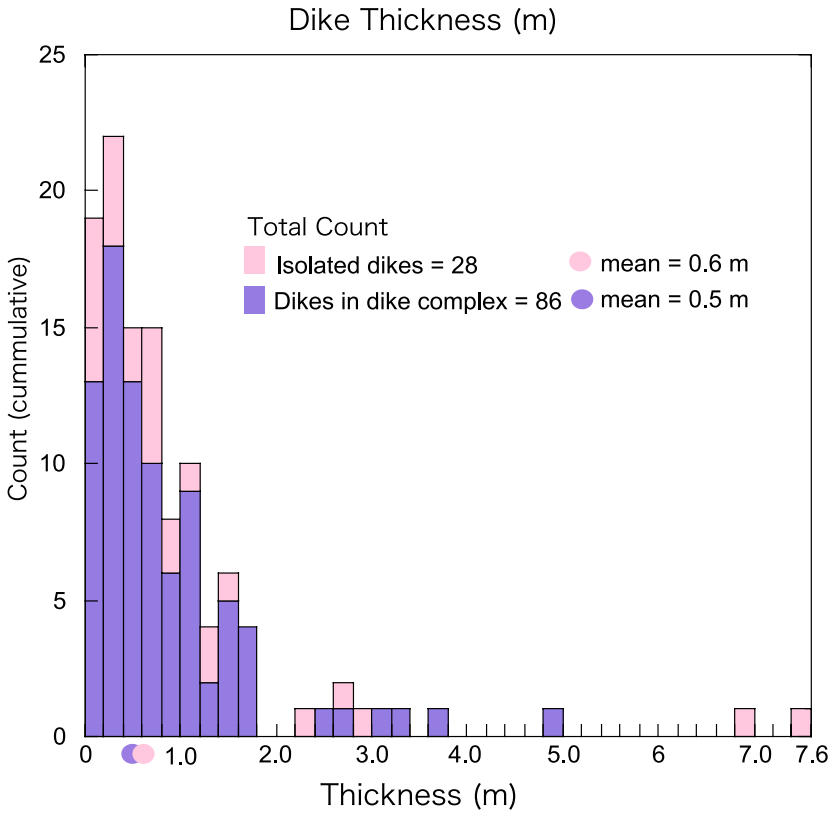

B.

Figure 11. (a) Blue and pink dots indicate identified subvertical contacts of dikes in dike complex and isolated dikes, respectively, from FMS images. (b) Frequency distribution of dike thicknesses from the isolated dikes (blue) and the dikes in the sheeted dike complex (pink).

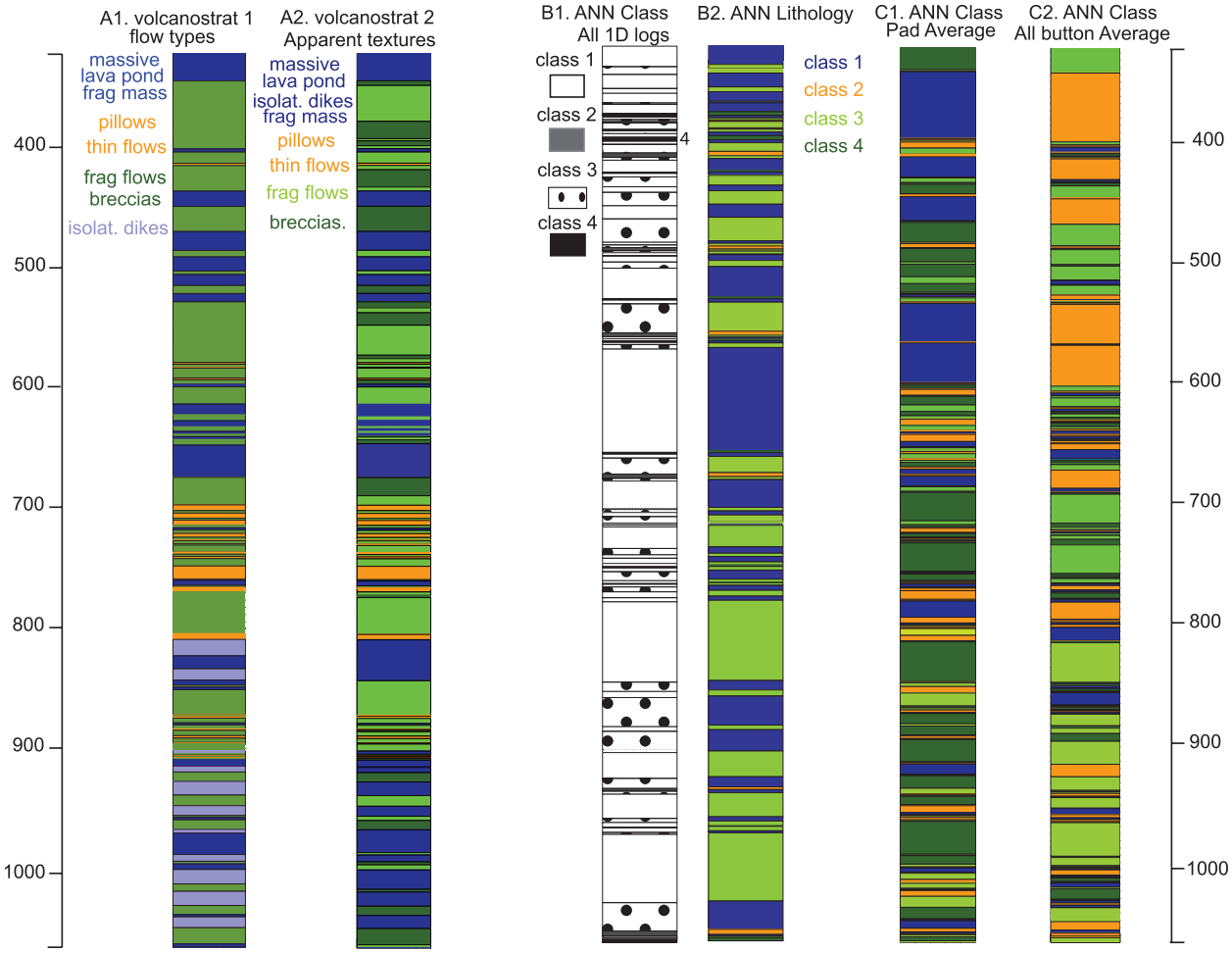

Figure 12. Simplified volcanostratigraphy models from electrofacies analysis and selected plots from ANN analyses. Group A1 shows a simplified volcanostratigraphy model following flow types. Colored letters correspond to stratigraphic layers with same color. Group A2 shows simplified volcanostratigraphy model following apparent texture types. Colored letters correspond to stratigraphic layers with same color. Group B1 shows ANN classification results with our choice of parameters (see section 6.2 for details). Classes 1∼4 are displayed with different patterns. Group B2 shows ANN lithology based on the comparison between groups A2 and B1. Color coding follows lithologies in group A1 model (see section 6.3 for details about the correlations). Group C1 shows an example of ANN results with FMS pad averages. Sixteen buttons on one pad were averaged into a pad average value at a sampling depth. Group C2 shows an example of ANN results with FMS button averages. Sixty four buttons on all (four) pads were averaged in a button average value at a sampling depth. Color coding of C1 and C2 models follows B2.

tigraphy, but cooling unit thickness was the only criteria used on shipboard to distinguish pillows from massive flows [*Plank et al.*, 2000]. *Barr et al.* [2002] lumped the shipboard "pillows" and "pillows or flows" units together as pillow. Some pillow units in the shipboard lithostratigraphy of Hole 801C (e.g., those associated with the two hydrothermal deposits) have clear characteristics of pillows in the recovered drill cores, core photographs, and the visual core descriptions, including subvertical and irregular curved glassy margins in addition to subhorizontal curved chilled margins [*Plank et al.*, 2000; J. Alt, personal communication, 2008]. In contrast, Cores 34–36 and 38–39, which in the shipboard lithostratigraphy figures [*Plank et al.*, 2000] and Figure 12 in the work of *Barr et al.* [2002] are plotted as exclusively pillows, contain only horizontal to subhorizontal chilled margins, consistent with thin flows or possibly with pillows. These units lack any hyaloclastite or clear tiny pillow fragments, or subvertical curved chilled glassy margins that would favor their interpretation as pillow basalts. Moreover, in the shipboard visual core descriptions, most of the

cooling units in Cores 34–36 and 38–39 are classified as "flows" and "pillows or flows, "with only a few cooling units described as "pillows" on the basis of their thickness less than 0.5 m [*Plank et al.*, 2000]. Thus the available evidence suggests that Cores 801C 34–36 and 38–39 are better classified as thin flows than as exclusively pillows. On the basis of our criteria for FMS image/electrofacies analysis developed for Hole 1256D, many of the purported "pillows" in the Hole 801C volcanostratigraphy would be instead classified as thin flows/thick pillows or fragmented flows.

[37] To explore other indications for the occurrence of pillow lavas, we examined whether the distribution of basaltic glass recovered downhole correlates with our identification of pillow lavas in Hole 1256D. Glass was most commonly recovered from the upper and middle parts of Hole 1256D (350–1050 and 1150–1250 mbsf) and corresponds to several rock types, such as fragmented flows, breccias, and pillow lavas (Figure 4). However, all such flow styles will develop a few centimeters of surficial glass when they interact with cold seawater and hence, glass recovery is not a unique parameter for identifying pillow lavas. We also examined the radius of curvature of curvy textures identified in the FMS images to investigate whether this can be utilized to identify pillows; however, this is also not a definitive parameter as the size of pillows in submarine environments can vary from 0.1 (knobby pillows) to a few meters (elongate/bulbous pillows) [e.g., *Lonsdale and Spiess*, 1980].

[38] We conclude that classifying flow types for a volcanostratigraphy model based on electrofacies analyses better relies on criteria that are principally based on the morphology of FMS images with good lateral coverage of the borehole wall. For pillows these features include closely packed, downward drooping tear drop shapes, radial fractures, highly conductive interpillow materials, and high conductivity irregular alteration patches (Figure 9). Some fragmented flows resemble these morphologies, but generally also display smaller scale, mesh-like fracturing systems (scale of fracturing a few ~10 cm)(Figure 7b).

[39] Implementation of the above criteria has led to a thorough revision of the occurrence of pillow lavas from that proposed in the Hole 1256D shipboard stratigraphy (364 and 788.8 mbsf) with new intervals of pillow lavas being identified and previously recognized intervals being reclassified as other rock types. A number of 1 to 10 m-thick intervals that satisfy our pillow lava criteria in the FMS and UBI images occur between 700 and 810 mbsf. These rocks were classified as sheet flows in the onboard observations [*Teagle et al.*, 2006].

5.2. Fragmented Flows and Breccias

[40] The porosity and permeability structure of the upper oceanic crust is critically important to understanding hydrothermal alteration processes [e.g., *Alt et al.*, 1986, 1996; *Alt*, 2004; *Fisher*, 2004; *Fisher et al.*, 2005]. Fluid flow and chemical exchange are tightly linked to the bulk porosity of the crust and the distribution of highly fractured and brecciated rock types. However, such intervals are commonly absent or very poorly represented in cores recovered by ocean drilling and hence their distribution must be determined from wireline criteria. This is a major hindrance to investigations of seawater-basalt chemical exchange because these intervals endure the most intensive hydrothermal alteration in the oceanic crust. We propose three different physically altered, fragmented lithofacies in our volcanostratigraphy: fractured massive flows, fragmented flows, and breccias. Overall, these three flow types make up more than 40% of Hole 1256D and more than 50% of the volcanic sequences (Table 3 and Figure 4). We used the term "fragmented" to indicate fractures that may have been physically developed through construction of the upper oceanic crust. From electrofacies analysis, we suggest that the range of fragmented flows observed downhole is best separated, rather than grouped together as "breccias," as in previous studies [e.g., *Barr et al.*, 2002]. This is because the degrees of fragmentation and the volcanic origins of flows can be different, and these are clearly discernible from the wireline images.

[41] Each lithofacies shows a different distribution downhole. The majority of fractured massive flows occur between 625 and 675 mbsf. Fragmented flows are regularly distributed between 350 and 950 mbsf and breccias are concentrated in the upper (350–700 mbsf) and lower (925–1065 mbsf) parts of the extrusive section (Figure 4). Fractured massive flows and fragmented flows show areas of relatively homogeneous texture similar to that displayed in intervals of massive flows or thin flow/thick pillows. These flows, hence, may have originally comprised a variety of relatively high effusion-rate flows such as lobate, wrinkled, jumbled, lineated sheet flows as are commonly observed at the EPR ridge crest [*Fornari et al.*, 1998, 2004]. The fragmentation (faulting) could be induced during cool-

ing/quenching, due to lava loading, or local and/or regional tectonics before chemical alteration [e.g., *Escartín et al.*, 2007].

[42] The origin of Breccias appears to be different from other fragmented rock types because brecciated intervals are completely fragmented and any primary volcanic textures, if ever present, are destroyed. We attribute these highly fragmented intervals to such features as shattered pillows caused by landsliding on slopes [*Moore*, 2001], collapsed pits among lobe/inflated flows [*Umino et al.*, 2000], collapsed lava pillars [*Perfit et al.*, 2003], and sagged lava channels [*Soule et al.*, 2005].

5.3. Lava-Dike Transition Zone

[43] The boundary between lava sequences and the sheeted dike complex in both ophiolites and intact ocean crust is laterally and stratigraphically transitional with a change from <10% to >90% dikes commonly occurring over a vertical distance of ~100 m [e.g., *Gass*, 1960; *Wilson*, 1959; *Hooft et al.*, 1996]. In Hole 504B this transition, as determined by core descriptions, occurs between 572 and 781 msb [*Alt et al.*, 1996] and marks a zone over which there are major changes in crustal physical properties (e.g., permeability) [*Becker*, 1989] and hydrothermal alteration.

[44] In Hole 1256D the upper boundary of the transition zone was placed at 1004.2 mbsf (Core 1256D-117R-1, 85 cm) because of the first presence in the cores of isolated dikes and the occurrence of subgreenschist facies secondary alteration minerals [*Teagle et al.*, 2006]. However, the low recovery rates in Hole 1256D, especially from brecciated intervals and fracture fillings, means that the exact shallowest in situ depth of the subgreenschist facies minerals remains uncertain. Unfortunately, there are not significant changes in the wireline logs at this level and the precise position of the upper boundary of the transition zone in Hole 1256D remains equivocal.

[45] The lower boundary of the transition zone at 1061 mbsf was assigned based on shipboard petrological observations of recovered core pieces [*Teagle et al.*, 2006]. Electrofacies analysis suggests that the lowermost fractured massive flow and massive flow occurs at 1064 mbsf. The corresponding recovered core comprises only short core pieces (Core 1256D-128R1 Piece 16–21) consistent with being from the lowermost fractured massive flow (1061–1064 mbsf) (Table S1 and Figure 8). Dikes are observed as the dominant rock type below this depth in both the drill core and the wireline logs, with gradational changes in wireline physical properties, particularly increases in LLD and LLS values. Therefore we propose 1064 mbsf as the lower boundary of the transition zone in our new crustal stratigraphy.

6. Toward an Objective, Quantitative Volcanostratigraphy

[46] In addition to the qualitative electrofacies analysis above, we carried out an alternate approach to construct a completely objective, quantitative volcanostratigraphy by using an unsupervised ANN method. An ANN is a computer algorithm designed following the information transportation and interpretation systems of the human brain. The principal abilities of ANN are the adaptive classification, prediction, and correlation of input information. ANN approach has advantages superior to other classification techniques (e.g., K-means clustering, discriminant analysis) as there is no need for prescreening of outliers or scaling input data sets following theoretical mechanisms. Without prerequisite knowledge of the logic behind a problem or behavior, ANN can act as a nonparametric, nonlinear regression technique so that we do not have to know how the data will be fitted by the modeling before the calculation [*Dowla and Rogers*, 1995]. This nature of ANN makes it possible to sort data into an almost unlimited desired number of classes. In any classification technique, one may wish to determine the number of significant discriminant groups, and in the case of ANN, we determine the number of classes (neurons). ANN technique is potentially of great value for the analysis of multiple parameter observations such as downhole wireline logs. If successful, a quantitative crustal stratigraphy could be constructed by classifying rock types or eruptive styles based solely on distinctive ranges of numerical logging parameters.

[47] ANN algorithms are broadly classified into two groups: supervised and unsupervised. Supervised ANN requires three steps in the task of classification. The first stage is "training" where a network is trained using input and desired output data sets. Next, the trained network is tested on examples it has not seen. Last, the successfully trained network is applied to new data sets and classifies the data into designated groups [e.g., *Dowla and Rogers*, 1995]. In contrast, unsupervised ANN analyzes input data without predetermined output targets. The unsupervised network

classifies input data into designated numbers of classes by finding clusters or similarities within the data based on topological mapping [*Dowla and Rogers*, 1995].

[48] ANN approaches have been used in the petroleum industry to map hydrological properties within reservoirs (e.g., porosity, permeability) or environmental test sites [e.g., *Link and Blundell*, 2003]. ANN have been only rarely applied in scientific ocean drilling [e.g., *Benaouda et al.*, 1999; *Moritz et al.*, 2000; *Goutorbe et al.*, 2006] and only once to examine downhole lithostratigraphy. Hole 792E located in the Izu-Bonin forearc comprises a sequence of volcanoclastic sandstones, conglomerates and claystones [*Taylor et al.*, 1990] drilled on Leg 126 with relatively high rates of recovery (>50%). Wireline data from this site were analyzed using supervised ANN routines where predetermined combinations of ANN classes had been calibrated against the rock types known from the recovered cores. ANN analysis performed better than other automated classification and feature detection techniques (e.g., discriminant analysis) in constructing a downhole lithostratigraphy [*Benaouda et al.*, 1999].

[49] Previous to our study, there has been no attempt to deploy ANN to analyze wireline logs of a highly fractured and variable substrate such as oceanic volcanic basement. Here we attempt to establish a quantitative volcanostratigraphy directly from wireline logs using an unsupervised ANN to test whether such an approach could be applied to rapidly construct a preliminary continuous downhole stratigraphy analysis, as would be useful aboard ship directly following wireline logging operations.

6.1. Application of Artificial Neural Network

[50] The self-organizing feature map (SOFM) [*Kohonen*, 1987] is an unsupervised ANN method and an example of a competitive network in which the number of classes or groups are user-defined input to the ANN system. The ANN classifies data by receiving input data and establishing stable boundaries (the number of boundaries equals the user-defined number of classes) among the input data. Weight vectors that correspond to the number of classes are initially set to random values. Once the boundaries become stable, these can delineate unknown input as the training stage is done [*Hagan et al.*, 1996]. This style of unsupervised network may be useful for constructing a quantitative volcanostratigraphy because it requires little input or bias from the interpreter and should achieve a completely objective output.

6.2. Methodology for Building Quantitative Lithostratigraphy

[51] We have employed an unsupervised SOFM to classify logging parameters from Hole 1256D to construct a quantitative volcanostratigraphy model. The calculation subroutines were programmed with the MATLAB® neural network toolbox. An unsupervised approach was used to avoid biasing the lithological classification, as would result if we employed a supervised approach with predetermined lithologic classifications based on the incomplete information yielded by the recovered cores.

[52] We first reexamined the volcanic section of our qualitative electrofacies analysis of Hole 1256D to build a simplified template lithostratigraphy of the hole for later comparison with our ANN output. We propose two different grouping of the rock types from our volcanostratigraphy model. In the first grouping the eight electrofacies in the volcanic section are clustered based on rock types observed from the fast spreading EPR crust: massive sheet flows, fragmented flows, pillow lavas, and breccias [e.g., *Fornari et al.*, 1998, 2004; *Bartetzko et al.*, 2002] into four major groups (R1) massive flows, massive off-axis ponded lava, and fractured massive flows; (R2) pillow lavas and thin flows; (R3) fragmented flows and breccias; and (R4) isolated dikes (Figure 12, group A1). In the second grouping elctrofacies are clustered based on similar textures on the FMS images into four major groups: (T1) massive flows, massive off-axis ponded lava, fractured massive flows, and isolate dikes; (T2) pillow lavas and thick pillow/thin flows; (T3) fragmented flows; and (T4) breccias (Figure 12, group A2). The major difference between these two templates is the treatment of isolated dikes (Figure 12, group A1) and breccias (Figure 12, group A2) as independent subdivisions.

[53] For the input data set to the ANN calculations, we used all the available one-dimensional wireline logs including LLD, LLS, NGR, density, porosity, Vp, and photoelectric effect factor measurements. We found that the combination of all wireline logging responses provided the most complete description of the in situ physical properties of the crust penetrated by Hole 1256D, following numerous trial-and-error examinations of different combinations of the numbers and types of wireline logs.

Table 4. Mean Values and Standard Deviations for ANN Classes[a]

Class	LagLLD (ohm m)	LogLLS (ohm m)	API (count)	Porosity (%)	Density (g/m^3)	Vp (m/s)	PEF (barns/e^-)
1	1.2 ± 0.4	1.1 ± 0.4	4.7 ± 1.8	30.8 ± 19.1	2.5 ± 0.4	4.6 ± 0.8	3.1 ± 0.8
2	1.6 ± 0.4	1.5 ± 0.4	4.0 ± 2.1	20.4 ± 16.0	2.7 ± 0.3	5.3 ± 0.6	3.2 ± 1.0
3	1.5 ± 0.4	1.4 ± 0.5	4.9 ± 2.9	23.4 ± 19.8	2.6 ± 0.4	5.1 ± 0.6	3.2 ± 1.0
4	1.5 ± 0.5	1.4 ± 0.5	4.0 ± 2.2	30.1 ± 25.4	2.6 ± 0.4	5.2 ± 0.8	3.1 ± 1.1

[a] Note that these values are calculated from wireline log from Expedition 312. Entire examined depth is 325–1064 mbsf.

[54] To use the Hole 1256D wireline logs, we first interpolated all logs from 312 to 1064 mbsf to a 0.15 m sampling interval to create common sampling depth profiles. This is necessary because different wireline tools analyze the borehole walls over different depth ranges. Since we proposed two different groupings of four rock types or FMS morphologies, the number of classes in the ANN calculation was set for four.

[55] We used a boxcar filter for smoothing and finalizing the ANN classification. Smoothing of the results is an important process in the application of SOFM to problems where fine-scale variation is the norm. If a smoothing filter is not applied the SOFM results are dominated by high-frequency variations in the input logs that emphasize the gradations from one class to the other and inhibit interpretation. It should be noted that when larger numbers of output classes are used, the resulting classifications often show smooth gradations from one class to the other [*Link and Blundell*, 2003]. To find the best smoothing filter size, we carried out numerous trial calculations in SOFM in pursuit of the best match between the output classes and our qualitative electrofacies volcanostratigraphy. After trials, we concluded that a sliding window of 33 points (~ 5 m) is most appropriate to evaluate the wireline logs in the ANN training routine. Use of a sliding window allows the network to look at data before and after each analysis point. A ~5 m window is close to the length of an IODP half-core which was the typical advance during drilling Hole 1256D. This approach is then similar to the observation and comparison techniques used by human interpreters of both cores and wireline logs.

6.3. Results: Quantitative ANN-Based Volcanostratigraphy

[56] The resulting four ANN classes (hereafter classes A1 to A4) represent different characteristics of in situ rock formation in Hole 1256D. The classification was calculated based on the combinations of all the wireline logs responses at a given depth by the SOFM program with aforementioned parameters.

[57] The ANN classification that resulted from using our selection of the parameters indicates that the order of the abundance (total thickness) of classes is class A1 > class A3 > class A2 ≈ class A4 (Figure 12, group B1 and Table 4). Overall, the distribution of these classes downhole comprises relatively thick intervals of classes A1 and A3 with thinner layers of classes A2 and A4. Very thick intervals of class A1 from 550 to 650, from 750 to 850, and from 950 to 1030 mbsf are distinctive. The thin layers of classes A2 and A4 show two different styles of distribution. Class A4 layers are commonly associated with class A3, and class A2 layers are found in thick class A1 and A3 layers. A set of logging tool responses of a class suggests characteristics of the in situ formation (Table 4). Class 1 is the formation characterized by low porosity, low NGR, and high Vp, indicating little fractured, less altered formation. In contrast, class 4 is the formation characterized by high porosity, high NGR, and low Vp, indicating very fractured, highly altered formation. Classes A2 and A3 are the formations characterized in between class 1 and 4 formation types, indicating transitional layers between classes A1 and A4. Provided the most distinctive difference between classes A2 and A3 are the NGR values, we suggest that class A2 formation is less altered than class A3 formation.

[58] Comparing the abundance, distribution, and set of logging responses of the ANN classes helps determine the representation of each class in terms of lithology. We tried matching ANN classes with lithologies using the FMS textural (Figure 12, group A2) volcanostratigraphy because the distribution of the ANN classes is most similar to the volcanostratigraphy model resulting from the FMS textural style types (T1–T4) as opposed to the flow types (R1–R4). The distribution of thick layering of massive flows (T1) from middle to lower part of the hole is almost identical to the distribution of ANN class A1. Together with the end-member

physical property characteristics of class A1 formations, we suggest that class A1 represents massive flows and less fractured portions of other flows, such as thin flows and fragmented flows. Correlating the ANN classes to lithologies is more challenging for class A2 that occur as thin layers between the massive flows and breccias or as localized thin layers. We suggest that class A2 is not a specific lithology but represent zones of anomalous porosity within class A1 formation. The distribution of class A3 is roughly the same as that of fragmented flows (T3) and breccias (T4). Together with other characteristics of class A3 formations, we suggest that class A3 represents both fragmented flows and breccias. The abundance of class A4 is very low and the distribution of this class is rare and seen as thin layers within class A3. Because the other characteristics of class A3 formations are in opposite sense from that of class A1, we suggest class A4 represents no lithology but zones of great degree of fragmentation and alteration within both fragmented flows and breccias.

[59] Some limitations of this approach are illustrated by the assignment of thick intervals of class 1 (massive flows) around 550–650 and 750–850 mbsf that correspond to significant intervals of fragmented flows as identified by our qualitative electrofacies-derived volcanostratigraphy. The wireline responses of fragmented flows in this interval do not contrast strongly with those of massive flows and the ANN could not detect class A3 around these depths. The ANN hence classified these rocks as class A1 instead, highlighting the difficulties of decision making when the ANN encounters intermediate properties.

6.4. Discussion: Applicability of ANN Modeling

[60] The ANN-based stratigraphy (Figure 12, group B2) more closely resembles our simplified electrofacies-derived volcanostratigraphy where rock types were clustered by textural style (Figure 12, group A2) as opposed to lava flow type (Figure 12, group A1). This points us toward the key properties that our ANN actually classifies. Local fracture systems and other controls on the bulk porosity (e.g., flow boundaries, breccias) have greatest influence on the resistivity distributions that lead to our interpretations of the FMS images. Bulk porosity is the primary parameter for many other crustal physical properties and imparts a major influence on the physical and chemical processes in the basement [*Alt*, 2004], and should have ranges that are distinctive from one rock type to another. There is a progressive increase in porosity from ANN class 1 to class 4, indicating that the local wall rock porosity has the strongest influence on our ANN classification.

[61] The distribution of porosity structures, particularly class 2 with intermediate porosities, may help us decipher lava depositional environments. Thin interlayers of class 2, associated with relatively thick intervals of class 1, appear to be porosity transitions from one end-member to another. Such porosity transitions are commonly observed at ocean ridges at the top and base of massive flows (class 1) with associating volcanic breccias (autobrecciation) (class 2). For example, such structures would be observed at the base of a massive flow that had filled a preexisting collapse pit or where the termination of lava supply results in the sagging and development of unsupported carapaces likely to collapse at the top of a massive flow.

[62] Deeper in the hole, below 900 mbsf, classes A2 and A3 occur independently of classes A1 and A4, the sharp gradients in bulk porosity may be attributed to high effusion eruptions close to the ridge axis, where massive flows are deposited in thick layers but drain-back of lava creates thin lava crusts that can degrade to breccias. Our ANN method is most reliable for classifying rock types when there are sharp contrasts in porosity structures.

[63] Caution is warranted utilizing ANN where there are major irregularities in the borehole walls as is common in ocean basement drilling. Wireline tools commonly return incorrect readings from zones of extended borehole diameter because sensors are strongly influenced by seawater between the wireline tools and the borehole wall. Our ANN would interpret such a zone as a highly porous formation, resulting in a mismatch between the ANN results and our electrofacies analysis. During the manual electrofacies analysis cross-sectional irregularities in Hole 1256D can be carefully monitored by eyeball comparison of several wireline logs and affected data disregarded. Prerequisite quality control thresholds on the caliper log could be set in the ANN to exclude certain data in the wireline logs in zones of large borehole diameter. However, if we use the caliper logs to exclude too many of the irregularities in the borehole wall prior to ANN analysis, our classification outcomes become biased toward flow or porosity structures that correspond to the undisturbed borehole wall and more robust rock types. Nevertheless, we

propose that ANN modeling improves our overview of porosity structure of the basement section, which cannot be reconstructed from piecemeal core data, particularly in highly altered or fragmented formations that typically have very low recovery rates.

[64] To explore other possible quantitative ANN models, we experimented with the quantitative use of FMS data. The FMS tool has four pads each with 16 resistivity sensor buttons. We have calculated continuous downhole average values for each pad and a button average value where the readings of all 64 buttons are averaged. The former represents the four different resistivity paths and the latter represents the cross-sectional average of resistivity in Hole 1256D at a given depth. ANN stratigraphies calculated using only these averages are shown in Figure 12, groups C1 and C2, respectively. These models are very different from our qualitative electrofacies stratigraphy. FMS data are most useful when they are processed for the visualization purposes; otherwise, they just provide multiple pass measurements of resistivity along various paths similar to that returned by the one-dimensional resistivity tools. Using only one input parameter or multiple measures of the basically same parameters (FMS pads average) did not improve the ANN adaptability because the resulting classes are only dependent on changes in that parameter so the weight functions that require multiple parameters cannot be appropriately tuned.

7. Conclusions

[65] Conclusions we draw from this study are as follows:

[66] 1. The electrofacies analysis in this study indicated that continuous wireline log data linked with multiple FMS passes is imperative to compensate the low recovery in basement drilling. Multiple types of wireline logs can be combined to discern different flow types, rock formations, flow boundaries, and fracture geometries. Good borehole coverage with FMS images is particularly helpful for identifying the distribution of basement lithologies and structures. Assuming that boreholes are relatively circular and that tool passes follow different paths, whenever possible multiple runs of the FMS tool string should be attempted during ocean drilling expeditions, as increased borehole wall coverage provides major gains for the integration of recovered drill core and the wireline logs, and the development of representative basement volcanostratigraphies.

[67] 2. Our electrofacies analysis suggests the upper oceanic crust in Hole 1256D (325–1425 mbsf) can be classified into zones of massive flows, massive off-axis ponded lava, fractured massive flows, fragmented flows, sheet flows or thick pillows, pillows, breccias, isolated dikes, dikes in sheeted dike complex, and gabbros. Each rock type can be attributed to an original flow or unit morphology but commonly these have been physically altered by fracturing and/or chemically altered by hydrothermal circulation.

[68] 3. Evenly spaced subvertical contacts in dike section are observed in FMS images between 1100 and 1410 mbsf. This indicates that the dikes are "dikes in sheeted dike complex" as observed in ophiolites.

[69] 4. From our volcanostratigraphy, the lower boundary of the transition zone was determined at 1064 mbsf.

[70] 5. ANN methods primarily classify the basement with respect to its bulk porosity and alteration structures downhole. ANN modeling can improve our overview of the basement porosity structure which is not possible to reconstruct from the piecemeal information provided by the recovered cores, particularly in intervals of high fracturing and hydrothermal alteration that are typically poorly recovered.

Acknowledgments

[71] The authors greatly appreciate M. Reichow, S. Saito, and W. Sager, colleagues at IFREE/JAMSTEC, Yokosuka, Japan; Trevor Williams at Borehole Research Group, Lamont-Doherty Earth Observatory; Curtis Link; and loggers on Leg 206 and Exp.309/312 (Florence Einaudi, Steven Kittredge, and Javier Espinosa) for their help. We acknowledge efficient editorial handling by Vincent Salters. Constructive criticism from associate editor, Douglas Wilson, and two anonymous reviewers improved this manuscript. This research used data provided by the Ocean Drilling Program (ODP) and the Integrated Ocean Drilling Program (IODP). The IODP and ODP is sponsored by the U. S. National Science Foundation (NSF) and participating countries under management of Joint Oceanographic Institutions (JOI). Tominaga was supported by JOI/U. S. Science Support Program for IODP (USSSP-IODP); a 2007–2008 Schlanger Ocean Drilling Fellowship, which is part of the NSF-sponsored USSSP-IODP that is administered by JOI; and the Jane and R. Ken Williams '45 Chair of Ocean Drilling Science and Technology.

References

Alt, J. C. (2004), Alteration of the upper oceanic crust: Mineralogy, chemistry, and processes, in *Hydrogeology of the Oceanic Lithosphere*, edited by E. E. Davis and H. Elderfield, pp. 495–533, Cambridge Univ. Press, New York.

Alt, J. C., and D. A. H. Teagle (1999), The uptake of carbon during alteration of ocean crust mineralogy and chemistry, *Geochim. Cosmochim. Acta*, *63*, 1527–1535, doi:10.1016/S0016-7037(99)00123-4.

Alt, J. C., J. Honnorez, C. Laverne, and R. Emmermann (1986), Hydrothermal alteration of a 1 km section through the upper oceanic crust, deep sea drilling project hole 504B mineralogy, chemistry, and evolution of seawater-basalt interactions, *J. Geophys. Res.*, *91*, 10,309–10,336, doi:10.1029/JB091iB10p10309.

Alt, J. C., et al. (1996), Hydrothermal alteration of a section of upper oceanic crust in the eastern equatorial Pacific: A synthesis of results from Site 504(DSDP Legs 69, 70 and 83, and ODP Legs 111, 137, 140, and 148), *Proc. Ocean Drill. Program Sci. Results*, *148*, 417–434.

Barr, S. R., S. Revillon, T. S. Brewer, P. K. Harvey, and J. Tarney (2002), Determining the inputs to the Mariana Subduction Factory: Using core-log integration to reconstruct basement lithology at ODP Hole 801C, *Geochem. Geophys. Geosyst.*, *3*(11), 8901, doi:10.1029/2001GC000255.

Bartetzko, A., P. Pezard, D. Goldberg, Y.-F. Sun, and K. Becker (2001), Volcanic stratigraphy of DSDP/ODP Hole 395A: An interpretation using well-logging data, *Mar. Geophys. Res.*, *22*, 111–127, doi:10.1023/A:1010359128574.

Bartetzko, A. R., R. Pechnig, and J. Wohlenberg (2002), Interpretation of well-logging data to study lateral variations in young oceanic crust: DSDP/ODP Holes 504B and 896A, Costa Rica Rift, in *Geological Applications of Well Logs*, *AAPG Methods Explor.*, vol. 13, edited by M. Lovell and N. Parkinson, pp. 213–228, Am. Assoc. of Petrol. Geol., Tulsa, Okla.

Bartetzko, A., H. Paulick, G. Iturrino, and J. Arnold (2003), Facies reconstruction of a hydrothermally altered dacite extrusive sequence: Evidence from geophysical downhole logging data (ODP Leg 193), *Geochem. Geophys. Geosyst.*, *4*(10), 1087, doi:10.1029/2003GC000575.

Bartetzko, A., N. Klitzsh, G. Iturrino, S. Kaufhold, and J. Arnold (2006), Electrical properties of hydrothermally altered dacite from the PACMANUS hydrothermal field (ODP Leg 193), *J. Volcanol. Geotherm. Res.*, *152*, 109–120, doi:10.1016/j.jvolgeores.2005.10.002.

Becker, K. (1989), Measurement of the permeability of the sheeted dikes in Hole 504B, ODP Leg 111, *Proc. Ocean Drill. Program Sci. Results*, *111*, 317–328.

Benaouda, D., G. Wadge, R. B. Whitmarsh, R. G. Rothwell, and C. MacLeod (1999), Inferring the lithology of borehole rocks by applying neural network classifiers to downhole logs: An example from the Ocean Drilling Program, *Geophys. J. Int.*, *136*, 477–491, doi:10.1046/j.1365-246X.1999.00746.x.

Dowla, F. U., and L. L. Rogers (1995), *Solving Problems in Environmental Engineering and Veosciences With Artigicial Neural Networks*, 239 pp., MIT Press, Boston.

Escartín, J., S. A. Soule, D. J. Fornari, M. A. Tivey, H. Schouten, and M. R. Perfit (2007), Interplay between faults and lava flows in construction of the upper oceanic crust: The East Pacific Rise crest 9°25–9°58N, *Geochem. Geophys. Geosyst.*, *8*, Q06005, doi:10.1029/2006GC001399.

Fisher, A. T. (2004), Rates of flow and patterns of fluid circulation, in *Hydrogeology of the Oceanic Lithosphere*, edited by E. Davis and H. Elderfield, pp. 337–375, Cambridge Univ. Press, New York.

Fisher, A. T., T. Urabe, A. Klaus, and the Expedition 301 Scientists (2005), *Proceedings of the Integrated Ocean Drilling Program*, vol. 301, Ocean Drill. Program, College Station, Tex.

Fisher, N. I., T. Lewis, and B. J. J. Embleton (1987), *Statistical Analysis of Spherical Data*, 329 pp., Cambridge Univ. Press, Cambridge, U. K.

Fornari, D. J., R. M. Haymon, M. R. Perfit, T. K. P. Gregg, and M. H. Edwards (1998), Axial summit trough of the East Pacific Rise 9°–10°N: Geological characteristics and evolution of the axial zone on fast spreading mid-ocean ridges, *J. Geophys. Res.*, *103*, 9827–9855, doi:10.1029/98JB00028.

Fornari, D., et al. (2004), Submarine lava flow emplacement at the East Pacific Rise 9°50N: Implications for uppermost ocean crust stratigraphy and hydrothermal fluid circulation, in *The Thermal Structure of the Ocean Crust and the Dynamics of Hydrothermal Circulation*, *Geophys. Monogr. Ser.*, vol. 148, edited by G. R. Foulger and D. M. Jurdy, pp. 187–218, AGU, Washington, D. C.

Gardener, J. S., and J. L. Dumanoir (1980), Litho-density log interpretation, *Trans. SPWLA Annu. Logging Symp.*, *21*, 1–23.

Gass, I. G. (1960), The geology and mineral resources of the Dhali area, *Mem. Geol. Surv. Dept. Cyprus*, *4*, 16 pp.

Gillis, K. M., and K. Sapp (1997), Distribution of porosity in a section of upper oceanic crust exposed in the Troodos Ophiolite, *J. Geophys. Res.*, *102*, 10,133–10,149, doi:10.1029/96JB03909.

Goutorbe, B., F. Lucazeau, and A. Bonneville (2006), Using neural networks to predict thermal conductivity from geophysical well logs, *Geophys. J. Int.*, *166*, 115–125, doi:10.1111/j.1365-246X.2006.02924.x.

Hagan, M. T., H. B. Demuth, and M. Beale (1996), *Neural Network Design*, 736 pp., PWS Publ., Boston, Mass.

Haggas, S. L., T. S. Brewer, P. K. Harvey, and G. I. Iturrino (2001), Relocating and orientating cores by the integration of electrical and optical images: A case study from Ocean Drilling Program Hole 735B, *J. Geol. Soc.*, *158*, 615–623.

Haggas, S. L., T. S. Brewer, and P. K. Harvey (2002), Architecture of the volcanic layer from the Costa Rica Rift, constraints from core-log integration, *J. Geophys. Res.*, *107*(B2), 2031, doi:10.1029/2001JB000147.

Hooft, E. E. E., H. Schouten, and R. S. Detrick (1996), Constraining crustal emplacement processes from the variation in seismic layer 2A thickness at the East Pacific Rise, *Earth Planet. Sci. Lett.*, *142*, 289–309, doi:10.1016/0012-821X(96)00101-X.

Kohonen, T. (1987), Adaptive, associative, anda self-organizing functions in neural computing, *Appl. Opt.*, *26*, 4910–4918.

Link, C. A., and S. Blundell (2003), Interpretation of shallow stratigraphic facies using a self-organizing neural network, in *Geophysical Applications of Artificial Neural Networks and Fuzzy Logic*, *Mod. Approaches Geophys.*, vol. 21, edited by W. Sandham and M. Leggett, pp. 215–230, Kluwer Acad., Boston, Mass.

Lonsdale, P., and F. N. Spiess (1980), Deep-tow observations at the East Pacific Rise, 8′ 45 N, and some interpretations, *Deep Sea Res.*, *54*, 43–62.

Macdonald, K. C., P. J. Fox, R. T. Alexander, R. Pockalny, and P. Gente (1996), Volcanic growth faults and the origin of Pacific abyssal hills, *Nature*, *380*, 125–129, doi:10.1038/380125a0.

Moore, J. G. (2001), Density of basalt core from Hilo drill hole, Hawaii, *J. Volcanol. Geotherm. Res.*, *112*, 221–230, doi:10.1016/S0377-0273(01)00242-6.

Moritz, E., S. Bornholdt, H. Westphal, and M. Meschede (2000), Neutral network interpretation of LWD data (ODP Leg 170) confirms complete sediment subduction at the Costa Rica convergent margin, *Earth Planet. Sci. Lett.*, *174*, 301–312, doi:10.1016/S0012-821X(99)00270-8.

Nielsen, S. G., M. Rehkämper, D. A. H. Teagle, D. A. Butterfield, J. C. Alt, and A. N. Halliday (2006), Hydrothermal fluid fluxes calculated from the isotopic mass balance of thallium in the oceanic crust, *Earth Planet Sci. Lett.*, *251*, 120–133.

Perfit, M. R., J. R. Cann, D. J. Fornari, J. Engles, D. K. Smith, W. I. Ridley, and M. H. Edwards (2003), Interaction of sea water and lava during submarine eruptions at mid-ocean ridges, *Nature*, *426*, 62–65, doi:10.1038/nature02032.

Pezard, P. A. (1990), Electrical properties of mid-ocean ridge basalt and implications for the structure of the upper oceanic crust in Hole 504B, *J. Geophys. Res.*, *95*, 9237–9264, doi:10.1029/JB095iB06p09237.

Plank, T., et al. (2000), *Proceedings of the Ocean Drilling Program, Initial Reports* [CD_ROM], vol. 185, Ocean Drill. Program, College Station, Tex.

Pockalny, R. A., and R. L. Larson (2003), Implications for crustal accretion at fast spreading ridges from observations in Jurassic oceanic crust in the western Pacific, *Geochem. Geophys. Geosyst.*, *4*(1), 8903, doi:10.1029/2001GC000274.

Purdy, G. M., L. S. L. Kong, G. L. Christeson, and S. C. Solomon (1992), Relationship between spreading rate and the seismic structure of mid-ocean ridges, *Nature*, *355*, 815–817, doi:10.1038/355815a0.

Révillon, S., S. R. Barr, T. S. Brewer, P. K. Harvey, and J. Tarney (2002), An alternative approach using integrated gamma-ray and geochemical data to estimate the inputs to subduction zones from ODP Leg 185, Site 801, *Geochem. Geophys. Geosyst.*, *3*(12), 8902, doi:10.1029/2002GC000344.

Rider, M. H. (1996), *The Geological Interpretation of Well Logs*, 280 pp., Gulf Publ., Caithness, U. K.

Smith, W. H. F., and D. T. Sandwell (1997), Global seafloor topography from satellite altimetry and ship depth soundings, *Science*, *277*, 1957–1962.

Soule, S. A. D. J. F., M. R. Perfit, M. A. Tivey, W. I. Ridley, and H. Schouten (2005), Channelized lava flows at the East Pacific Rise crest 9°–10°N: The importance of off-axis lava transport in developing the architecture of young oceanic crust, *Geochem. Geophys. Geosyst.*, *6*, Q08005, doi:10.1029/2005GC000912.

Taylor, B., et al. (1990), *Proceedings of the Ocean Drilling Program, Initial Reports*, vol.126, Ocean Drill. Program, College Station, Tex.

Teagle, D. A. H., J. C. Alt, and A. N. Halliday (1998), Tracing the chemical evolution of fluids during hydrothermal recharge: Constraints from anhydrite recovered in ODP Hole 504B, *Earth Planet. Sci. Lett.*, *155*, 167–182, doi:10.1016/S0012-821X(97)00209-4.

Teagle, D. A. H., M. J. Bickle, and J. C. Alt (2003), Recharge flux to ocean-ridge black smoker systems: A geochemical estimate from ODP Hole 504B, *Earth Planet. Sci. Lett.*, *210*, 81–89, doi:10.1016/S0012-821X(03)00126-2.

Teagle, D. A. H., J. C. Alt, S. Umino, S. Miyashita, N. R. Banerjee, D. S. Wilson, and the Expedition 309/312 Scientists (2006), *Proceedings of the Integrated Ocean Drilling Program*, vol. 309/312, pp. 1–127, U. S. Govt. Print. Off., Washington, D. C.

Umino, S., P. W. Lipman, and S. Obata (2000), Subaqueous lava flow lobes, observed on ROV KAIKO dives off Hawaii, *Geology*, *28*, 503–506, doi:10.1130/0091-7613(2000)28<503:SLFLOO>2.0.CO;2.

Umino, S., S. Obata, P. Lipman, J. R. Smith, T. Shibata, J. Naka, and F. Trusdell (2002), Emplacement and inflation structures of submarine and subaerial Pahoehoe lavas from Hawaii, in *Hawaiian Volcanoes: Deep Underwater Perspectives*, *Geophys. Monogr. Ser.*, vol. 128, edited by E. Takahashi et al., pp. 85–101, AGU, Washington, D. C.

Wilson, D. S. (1996), Fastest known spreading on the Miocene Cocos-Pacific plate boundary, *Geophys. Res. Lett.*, *23*, 3003–3006, doi:10.1029/96GL02893.

Wilson, D. S., et al. (2003), *Proceedings of the Ocean Drilling Program, Initial Reports*, vol. 206, Ocean Drill. Program, College Station, Tex.

Wilson, D. S., et al. (2006), Drilling to gabbro in intact ocean crust, *Science*, *312*, 1016–1020, doi:10.1126/science.1126090.

Wilson, R. A. M. (1959), The geology and mineral resources of the Xeros-Troodos area, *Mem. Geol. Surv. Dept. Cyprus*, *1*, 135 pp.